Alma Mater Studiorum – Università di Bologna

DOTTORATO DI RICERCA IN AUTOMOTIVE

PER UNA MOBILITÀ INTELLIGENTE

Ciclo XXXV

Settore Concorsuale: 09/C2

Settore Scientifico Disciplinare: ING-IND11 "Fisica Tecnica Ambientale"

ACTIVE CONTROL OF SOUND RADIATED BY VIBRATING SURFACES ON A MCLAREN SUPERCAR

Presentata da: Anna Tira

Coordinatore di Dottorato:

Chiar.mo Prof. Nicolò Cavina

Supervisore:

Chiar.mo Prof. Angelo Farina

Co-supervisore:

Dr. Daniel Pinardi

Esame Finale Anno 2023

To all the people that gave me the strength to carry on despite the very challenging number of difficulties that filled up this path.

In particular to my dear colleague and friend Dr. Daniel Pinardi.

CONTENTS

INDEX OF FIGURES

ACRONYM LIST

AAL	Accumulated Acceleration Level
B&K	Bruel&Kjaer
DUT	Device Under Test
ESS	Exponential Sine Sweep
FEM	Finite Element Method
FFT	Fast Fourier Transform
FIR	Finite Impulse Response
FRF	Frequency Response Function
IFFT	Inverse Fast Fourier Transform
IR	Impulse Response
LDV	Laser Doppler Vibrometer
NTF	Noise Transfer Function
SISO	Single-input Single-output
SPL	Sound Pressure Level
S/N	Signal to Noise Ratio

1.Introduction

Sound radiators based on forced vibrations of plates are becoming widely employed, mainly for active sound enhancement and noise cancelling systems, both in music and automotive environment. Nowadays, automotive industry really cares about sound quality of car cabins. On one side, customers demand for quieter interiors, on the other hand hybrid and full electric vehicles, being very silent, can cause inconveniences and danger in urban circulation as well as an unfamiliar feeling to the driver (especially in case of sport cars). Active sound enhancement solutions based on electromagnetic shakers hence find increasing interest. Mostly diffused applications deal with active noise control (ANC) and active vibration control systems for improving the acoustic experience inside or outside the vehicle. This requires investigating vibrational and, consequently, vibro-acoustic characteristics of vehicles. Traditionally, modal analysis and frequency response functions (FRFs) making use of impact hammers and accelerometers were employed. More recent and efficient non-contact methods are available, such as Laser Doppler Vibrometer (LDV) or Digital Image Correlation (DIC). They can both be adopted to study vibrations, even though DIC is mainly used for structural testing and material identification. At the same time, numerical simulations are more and more employed by car producers for improving the design of acoustics performances, reducing the need for expensive prototypes, and avoiding time-consuming measurements. Therefore, simulation and processing methods capable of reducing the calculation time and providing high-accuracy results, are strongly demanded.

The sound radiation of panels can be computed once the velocity of each point of the panel is known, as a response to the force applied in one or more positions. The analytical or numerical solution of the motion equation is so required and

depends on the boundary conditions. Numerous studies about the dynamic response of plates can be found in literature and the classical solution approaches are the Rayleigh-Ritz and superposition methods.

In this work, an ideal case study on rectangular plates in fully clamped conditions preceded a real case analysis on vehicle panels. The sound radiation generated by a vibrating flat or shallow surface can be calculated by means of Rayleigh's integral: it provides the solution of the sound pressure generated in one point in far field condition when the radiating surface operates in an infinite baffle. This means that the front and back radiation must be separated to avoid the influence of acoustic short circuits.

The analytical solution of the problem is here calculated implementing the equations in MATLAB. Then, the results are compared with a numerical model developed in COMSOL Multiphysics, employing Finite Element Method (FEM). To have truly comparable solutions, the input parameters (e.g., mesh and frequency resolutions, evaluation distance, material properties) are set equal. In both cases, the output consists in a chart of Sound Pressure Level (SPL) vs frequency.

A very good matching between analytical and numerical solutions is shown, thus the cross validation of the two methods is achieved. Furthermore, the problem of identifying the optimal application point of the exciting force is investigated, showing that the maximum A-weighted SPL is obtained applying the force at the center of the plate. In addition, a different optimization of the excitation point is performed, to provide the flattest frequency response. The models' validation was obtained through experimental laboratory measurements too.

The shift to the real case study, on a McLaren super car, led to the development of a mixed analytical-numerical-experimental method. The tested panel was the hood of a P14R. At first, the original geometry was simplified and slowly led to a correctly working numerical model. Then, experimental measurements were

carried out both with impact hammer and mini shakers emitting exponential sine sweeps (ESS), to evaluate the radiated SPL. To save computational time, the numerical COMSOL model was run without the acoustic module, determining only the vibrational response of the structure and post processing the mobility data in MATLAB, exploiting Rayleigh's formula. The best results were obtained with the mini shaker excitement, showing good matching of the recorded SPL with the calculated one over all the selected frequency band.

In addition, a set of directivity measurements of the hood were realized, to start studying the spatiality of sound, which is fundamental to active sound enhancement systems.

2. Theoretical background

2.1. Natural Frequencies and Modes of Vibration

Physical systems are spatially connected, and many contain non-uniformities of geometry or material properties. The presence of these boundaries affects the way waves propagate through them. Their interaction generates events such as refraction, diffraction, reflection, and scattering. All these phenomena can occur in solid structures, but the one having most practical importance is reflection. The reason for it is its responsibility for the existence of sets of frequencies (and associated patterns of vibration) which are proper to a bounded system. In practice, the interface could take the form of a boundary, a change of geometry or material, or a local constraint. For instance, an infinitely long, undamped beam can vibrate freely at any frequency; a constrained, undamped beam can vibrate freely only at discrete *natural* or *characteristic* frequencies, which are theoretically infinite in number. The elements of the beam that are not at boundaries satisfy the same equation of motion in both cases, but they only 'know about' the constraints because of the phenomenon of wave propagation and reflection. Reflection at boundaries also leads to a phenomenon of great importance: resonance. It must be underlined with careful attention that resonance is an event associated with *forced* vibration, generated by some input. Natural frequencies are instead associated with *free* vibration. So, if a system is subjected to a transient disturbance, one could ask which frequencies would be observed in the consequent vibration, and what spatial distribution of vibration would occur. When a freely propagating wave meets a region of the system in which the dynamic properties are different from those of the previously traversed one, a reflected wave is generated and, in combination with the incident wave, is in equilibrium with the transmitted wave that travels beyond the interface. Yet if

the beam ends at a free end or a fully clamped support, or by an element that doesn't dissipate or transmit energy, the amplitude of the reflected wave has to be equal to that of the incident wave. Therefore, such conservative terminations generate standing-wave interference patterns. These pure standing-wave fields occur in an undamped system in free vibration at frequencies known as *characteristic* or *natural* frequencies. The related spatial distributions of vibration amplitudes are called *characteristic functions* or *natural modes* of the system. The natural frequencies are function of the material properties and geometric dimensions of the considered element, and they are infinite in number in continuously distributed elastic systems. Hence, the reflection of undamped travelling waves from non-transmitting and non-dissipative boundaries, or from any type of discontinuity, creates an interference field that, if composed solely of undamped waves of a frequency equal to a natural frequency of the system, takes the form of a standing-wave field in which the associated distribution of vibration amplitude is characteristic of the system and is known as a characteristic function, or natural mode, of the system [1], [2].

2.2. Forced Vibration and Resonance

A linear elastic system subject to a stationary and continuous disturbance can vibrate in correspondence of the frequencies present in the perturbation and not just of the natural frequencies. Indeed, in some cases, they can be completely absent. The process can be clarified with a one-dimensional example. Suppose to have a pipe with a movable piston at one end, a rigid top on the other extremity and a microphone placed at a certain point in the tube. Displacing the piston impulsively inwards, an air pressure pulse travels down the tube, gets reflected at the final plug, travels back to the piston, reflects down the pipe and continues theoretically non-stop. A succession of pulses having a period of $\frac{2l}{c}$ (l is the tube's length and c is the sound's speed) are thus recorded by the microphone. Analyzing the signal in frequency domain, a spectrum with discrete lines would

appear, precisely at frequencies given by $f_n = n\frac{c}{2l}$, where n is any positive integer. These are the natural frequencies of the pipe. If the piston instead is impulsively displaced periodically at intervals of time T, the pulse pattern period at the microphone will be T, and the frequencies in the received signal will be m/T, where m is any positive integer. In spite of the fact that each pulse does a full trip in the same time as before, i.e. $2l/c$, the natural frequencies do not appear in the spectrum unless $m/T = nc/2l$, or $T/(2l/c) = m/n$. In this case, the exciting pulses reinforce certain reflections of previous pulses, and strong signal components at frequencies $f = m/T$ can be observed [1]. Such coincidence of excitation frequency and natural frequency, that leads to a reinforcement in the response, is defined 'resonance'. It is important to notice that resonant response is damping controlled: this can take form of material damping, interface damping or energy radiation into adjoining structures or fluids. The relation between the applied force and the resulting velocity at the driving point (the force application point), depends on two factors: the properties of the structure in the close vicinity of the driving point and the amplitude and phase at the driving point of any waves reflected to that point from discontinuities or constraints in the surrounding structure. The resonance phenomenon does not depend on the position of the excitation (except for a mode's nodal line). Structural damping can often be reasonably represented mathematically by attributing a complex elastic modulus to the material: $E' = E(1 + j\eta)$, where η is the so called 'loss factor' [3], which is normally much smaller than unity. For many structures η tends to decrease with frequency [3], [4].

2.3. Dynamic Response of Fully Clamped Isotropic Rectangular Plates

Numerous studies about dynamic response of plates with various boundary conditions can be found in literature where the classical solution approaches are the Rayleigh-Ritz and superposition methods [5]–[10]. The sound radiation of

vibrating plates can be calculated once the velocity of each point of the panel is known, as a response to the force applied in one or more points [11]–[20]. Therefore, the analytical solution of the motion equation is required and depends on the boundary conditions. For an undamped thin plate under the external excitation of a harmonic point force, the governing equation of bending vibrations [7], [10], [21] is:

$$B\left(\frac{\partial^4}{\partial x^4}+2\frac{\partial^4}{\partial x^2\partial y^2}+\frac{\partial^4}{\partial y^4}\right)w(x,y,t)+\rho h\frac{\partial^2 w(x,y,t)}{\partial t^2}=p_{ext}(x,y,t)$$

Eq. 1

where $B=\frac{Eh^3}{12(1-\nu^2)}$ is the bending stiffness of the plate, w is the displacement along the plate's normal direction (x,y), h is the plate thickness, ν is Poisson's ratio, ρ is the density of the plate material and p_{ext} is the applied harmonic force per unit area. It has angular frequency ω and acts on point (ξ,η) along the z-axis (positive). Letting so

$$w(x,y,t)=W(x,y)e^{i\omega t}$$

Eq. 2

and

$$p_{ext}(x,y,t)=P(x,y)e^{i\omega t}$$

Eq. 3

the equation is simplified as:

$$B\left(\frac{\partial^4}{\partial x^4}+2\frac{\partial^4}{\partial x^2\partial y^2}+\frac{\partial^4}{\partial y^4}\right)W(x,y)-\rho h\omega^2 W(x,y)-P(x,y)=0$$

Eq. 4

Expanding $W(x,y)$ and $P(x.y)$ as superposition of shape functions one obtains:

$$W(x,y)=\sum_{m=1}^{\infty}\sum_{n=1}^{\infty}W_{mn}\psi_{mn}(x,y)$$

Eq. 5

$$P(x,y) = \sum_{m=1}^{\infty}\sum_{n=1}^{\infty} P_{mn}\psi_{mn}(x,y)$$

Eq. 6

The Virtual Work Principle is written as:

$$\int_0^b \int_0^a [B\nabla^2\nabla^2 W(x,y) - \rho h\omega^2 W(x,y) - P(x,y)](\delta W)dxdy = 0$$

Eq. 7

where the virtual displacement δW is:

$$\delta W = \sum_{i=1}^{\infty}\sum_{k=1}^{\infty} \delta W_{ik}\psi_{ik}(x,y)$$

Eq. 8

and

$$\nabla^2\nabla^2 = \frac{\partial^4}{\partial x^4} + 2\frac{\partial^4}{\partial x^2 \partial y^2} + \frac{\partial^4}{\partial y^4}$$

Eq. 9

The shape function of Eq. 5 and Eq. 6 can be decomposed as:

$$\psi_{mn}(x,y) = X_m(x)Y_n(y)$$

Eq. 10

where X_m and Y_n are eigenfunctions that satisfy the boundary conditions of the plate (fully clamped, in this case) [7]. P_{mn} can be expressed as:

$$P_{mn} = \frac{\int_0^b \int_0^a P(x,y)X_m(x)Y_n(y)dxdy}{\int_0^b \int_0^a X_m^2(x)\, Y_n^2(y)dxdy}$$

Eq. 11

Substituting Eq. 5 and Eq. 6 in Eq. 7 one gets:

$$B\sum_i^{\infty}\sum_k^{\infty} W_{mn}\int_0^b \int_0^a \varphi_{ik}\nabla^2\nabla^2\varphi_{mn}dxdy - \rho h\omega^2\sum_i^{\infty}\sum_k^{\infty} W_{mn}\int_0^b \int_0^a \varphi_{ik}\varphi_{mn}dxdy - \sum_i^{\infty}\sum_k^{\infty} P_{mn}\int_0^b \int_0^a \varphi_{ik}\,\psi_{mn}dxdy = 0$$

Eq. 12

Using Eq. 10, Eq. 12 can be written as:

$$B\sum_i^m\sum_k^n W_{mn}\int_0^b\int_0^a[X_m^{(4)}Y_nX_iY_k + 2X_m''Y_n''X_iY_k + Y_n^{(4)}X_mX_iY_k]dxdy -$$

$$\rho h\omega^2\sum_i^m\sum_k^n W_{mn}\int_0^b\int_0^a X_mY_nX_iY_k\,dxdy = \sum_i^\infty\sum_k^\infty \frac{\int_0^b\int_0^a P(x,y)X_m(x)Y_n(y)dxdy}{\int_0^b\int_0^a X_m^2(x)Y_n^2(y)dxdy}\int_0^b\int_0^a X_mY_nX_iY_k\,dxdy$$

Eq. 13

The eigenfunctions $X_m(x), Y_n(y)$ and $X_i(x), Y_k(y)$ are orthogonal to each other so that:

$$\left.\begin{aligned}\int_0^a X_p(x)X_q(x)\,dx = \int_0^a X_p''(x)\,X_q''(x)dx = 0\\ \int_0^b Y_p(y)Y_q(y)\,dy = \int_0^b Y_p''(y)\,Y_q''(y)dy = 0\end{aligned}\right\},\ \ if\ p \neq q$$

Eq. 14

Eq. 13 can thus be simplified as:

$$B\sum_m\sum_n W_{mn}(I_1I_2 + 2I_3I_4 + I_5I_6) - \rho h\omega^2\sum_m\sum_n W_{mn}I_2I_6 = \sum_m\sum_n\int_0^b\int_0^a P(x,y)X_mY_n dxdy$$

Eq. 15

Where [21]:

$$I_1 = \int_0^a X_m^{(4)}X_m dx\ \ ;\ \ I_2 = \int_0^b Y_n^2 dy\ \ ;\ \ I_3 = \int_0^a Y_m''Y_m dx\ \ ;\ \ I_4 = \int_0^b Y_n''Y_n dy\ \ ;\ \ I_5 = \int_0^b Y_n^{(4)}Y_n dy\ ;\ I_6 = \int_0^a Y_m^2 dx$$

Eq. 16

Thus W_{mn} can be written as:

$$W_{mn} = \int_0^b\int_0^a P(x,y)X_mY_n dxdy/(B(I_1I_2 + 2I_3I_4 + I_5I_6) - \rho h\omega^2 I_2I_6)$$

Eq. 17

For a specific set of m and n values, for a concentrated load $P(\xi,\eta)$ Eq. 17 can be reduced to:

$$W_{mn} = \frac{PX_m(\xi)Y_n(\eta)}{D(I_1I_2 + 2I_3I_4 + I_5I_6) - \rho h\omega^2 I_2I_6}$$

Eq. 18

The dynamic response $W(x,y)$ of a plate subjected to a harmonic point force can therefore be expressed as:

$$W(x,y) = \sum_{m}^{\infty}\sum_{n}^{\infty} \frac{PX_m(\xi)Y_n(\eta)}{D(I_1I_2 + 2I_3I_4 + I_5I_6) - \rho h\omega^2 I_2 I_6} X_m(x)Y_n(y)$$

Eq. 19

2.4. Sound Radiation of Vibrating Plates: Rayleigh's Integral Method

Due to the perturbation on the surface of the plate and the consequent vibration, an acoustic pressure is generated in the space around and can be calculated by Rayleigh's integral [7], [22]–[26]:

$$P(\boldsymbol{r}_2) = \frac{j\omega\rho_0}{2\pi}\int_{dS} v(\boldsymbol{r}_1)\frac{e^{-jk|\boldsymbol{r}_2-\boldsymbol{r}_1|}}{|\boldsymbol{r}_2-\boldsymbol{r}_1|}dS$$

Eq. 20

where ρ_0 is the air density, ω is the angular frequency of the vibrations, k is the wave number, S is the plate surface and $|\boldsymbol{r}_2-\boldsymbol{r}_1|$ is the distance between the observation point and the measured one. The related sound pressure level can be obtained:

$$SPL(\boldsymbol{r}_2) = 20log\left(\frac{|P(\boldsymbol{r}_2)|}{p_0}\right)\ [dB]$$

Eq. 21

It is possible to discretize the rectangular plate into N elements of areas ΔS and thus to approximate the surface integral by a finite series of elements with known properties [23], [27]:

$$P(\boldsymbol{r}_2) = \frac{j\omega\rho_0}{2\pi}\sum_{n=1}^{N} v(\boldsymbol{r}_n)\ \frac{e^{-jk|\boldsymbol{r}_2-\boldsymbol{r}_n|}}{|\boldsymbol{r}_2-\boldsymbol{r}_n|}\Delta S_n$$

Eq. 22

It is also possible to define an accumulated acceleration:

$$aa(\boldsymbol{r}_2) = \frac{j\omega\rho_0}{2\pi}\int_{dS}\frac{|v(\boldsymbol{r}_1)|}{|\boldsymbol{r}_2-\boldsymbol{r}_1|}dS$$

Eq. 23

and the Accumulated Acceleration Level (AAL) [23]:

$$AAL(\boldsymbol{r}_2) = 20log\left(\frac{aa\big((\boldsymbol{r}_2)\big)}{p_0}\right)\ [dB]$$

Eq. 24

which neglects the phase information both from the displacement and the sound propagation from point $\boldsymbol{r}_1$ to point $\boldsymbol{r}_2$. Thus, the AAL summarizes the total vibration of the radiator from the energetic point of view. Both levels AAL and SPL are identical as long as all elements move in-phase (e.g., piston mode).

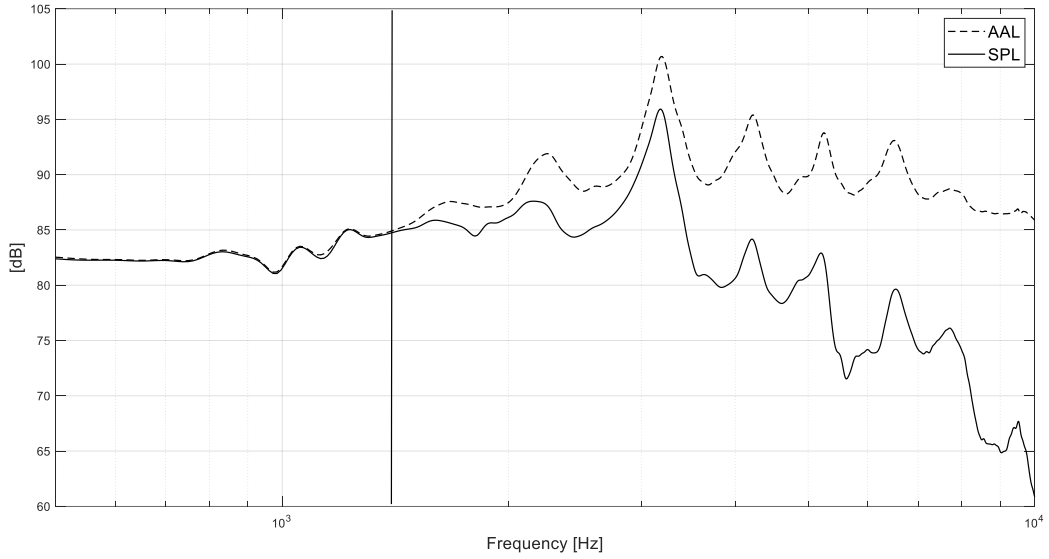

Figure 1: Example of a measurement output where AAL (dashed line) and SPL (solid line) are evaluated. It is visible how after the breakup (vertical line) they don't follow the same trend, being the AAL always higher than the SPL. Before the breakup the acoustic cancellation contribution is not present because of the piston mode displacement of the source.

2.5. Introduction to Impulse Response Measurement

The full information about the transfer function of a measured system is contained in its impulse response. Supposing the acoustic system to be linear and time invariant, named *x(t)* its input, *h(t)* its impulse response and *y(t)* its output, it can be written as [28]–[30]:

$$y(t) = x(t) \otimes h(t) = \int_{-\infty}^{+\infty} h(\tau)x(t-\tau)d\tau$$

Eq. 25

So, the output is given by the convolution between the input signal and the system's impulse response, namely by the integration of the product between *x(t)*

and *h(t)*, translated by a certain value τ. The main issue is how to "extract" the impulse response from the system once the input signal is set and the output is recorded. The first possibility consists in delivering to the system an impulsive test signal, so that the recorded output is the impulse response itself. Otherwise, a special input signal *x(t)* has to be employed, which must have an inverse function $x(t)^{-1}$ such that:

$$x(t) \otimes x(t)^{-1} = \delta(t)$$

Eq. 26

where $\delta(t)$ is a perfect impulse, namely Dirac's delta. The mathematical operation required to retrieve the Dirac's delta is called deconvolution, i.e. the inverse of the convolution, and it is denoted with the symbol $\otimes$.

In such case, it is possible to obtain the impulse response *h(t)* knowing the system's output and the *inverse filter* $x(t)^{-1}$ of the input *x(t)*. In formula:

$$h(t) = y(t) \otimes x(t)^{-1} = h(t) \otimes x(t) \otimes x(t)^{-1} = h(t) \otimes \delta(t)$$

Eq. 27

It can appear as an easy operation, but in practice it presents remarkable difficulties, such as the necessity of reproducing a sufficiently intense and short acoustic signal (at least 60 dB in terms of signal to noise ratio). It must be pointed out that the impulse response can be analysed for indoor environments or for solid structures. It means the techniques are different depending on the application. In this work structural impulse responses were investigated, for which direct and indirect measurement methods exist. The first classic technique is the impact hammer test (direct method) [31]–[34], which applies an impulsive force to the sample, and a valid alternative is the sweep excitation (indirect method) [29], [35], [36].

2.5.1. Impact Hammer measurements

A well-known and exploited type of test for modal analysis is the excitation of structures through an impact hammer [37], namely a hammer of variable

dimensions and weight, equipped with a load cell on its head to measure the applied impulsive force (Figure 2). Since the frequency range of interest can vary significantly, the load cell can be equipped with tips of different materials to act as mechanical (low pass) filters. Usually, rubber tips are applied when the excitation spectrum must be in low frequency. At the same time, small metal tips are needed if the frequency excitation band increases.

Figure 2: An impact hammer.

The stroke must be settled very precisely and with sufficient energy, to properly excite all the desired spectrum. Furthermore, the more the structure is stiff the more attention must be given not to double impact the excitation point: the surface's rebound can be so quick that the operator doesn't have the time to move away the hammer, producing a second lighter impact which compromises the measurement. Real-time analysis systems allow to immediately detect this type of error, managing to discard immediately the wrong inputs.

2.5.2. Exponential Sine Sweep technique

The Sine Sweep method consists in the generation of a pure tone that increases its frequency in time and is therefore reproduced by a loudspeaker or, for example, by an electrodynamic shaker placed on a stiff structure (that in this case acts as loudspeaker) [29], [35]-[38], [39]. Once the frequency band of interest is set for the analysis, a linear (Figure 3) or exponential trend (Figure 4) of this deterministic signal can be chosen. In the first case the signal has the same duration for each "swept" frequency, namely it progresses linearly in time. In the second case, the exponential growth of the tone makes it increase slowly at low

frequency and faster at high frequencies. The mathematical expressions of the two respective signals are as follows:

$$x(t) = \sin\left(\omega_1 t + \frac{t^2(\omega_2 - \omega_1)}{2T}\right)$$

Eq. 28

$$x(t) = sin\left[\frac{\omega_1 T}{ln\left(\frac{\omega_2}{\omega_1}\right)}\left(e^{\frac{t}{T}ln\left(\frac{\omega_2}{\omega_1}\right)-1}\right)\right]$$

Eq. 29

The sweeps start at angular frequency ω_1, end at angular frequency ω_2, taking T seconds.

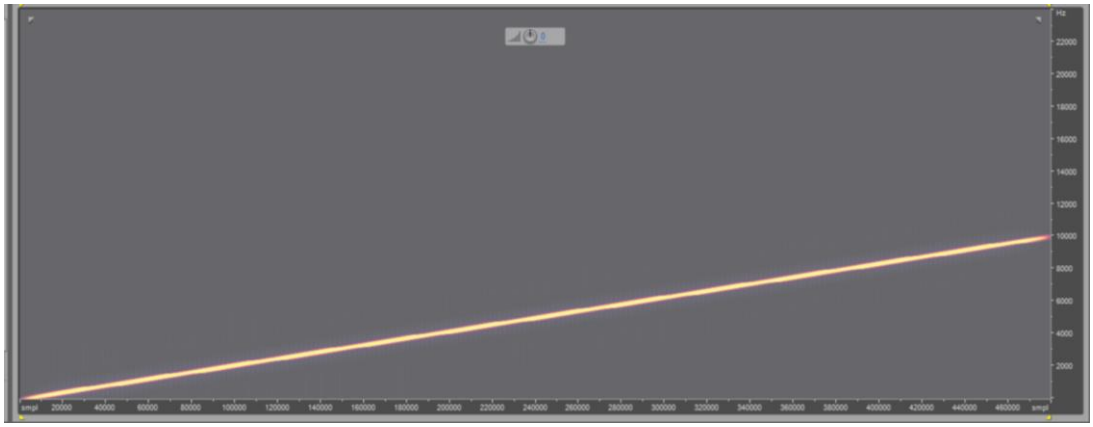

Figure 3: Spectral frequency display of a linear sine sweep.

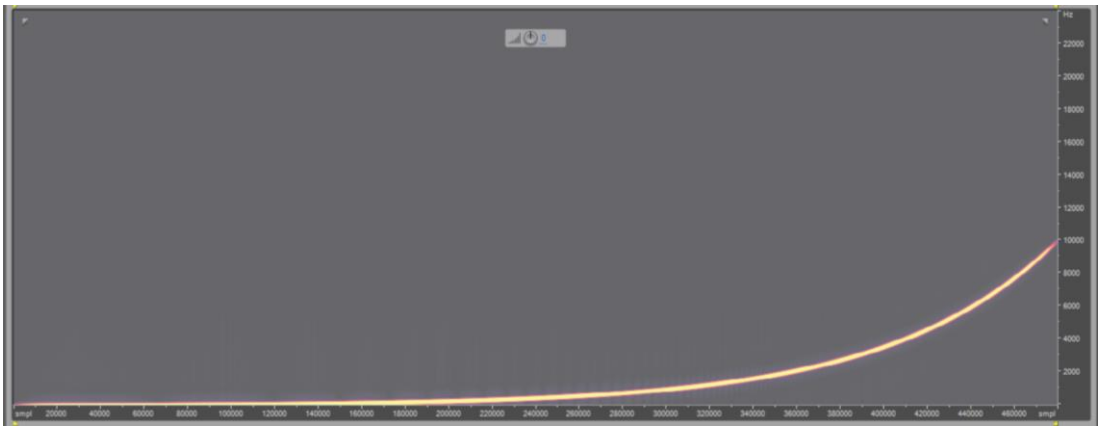

Figure 4: Spectral frequency display of an exponential sine sweep.

Using the Sine Sweep technique though, one does not introduce in the system an ideal unit impulse, therefore it's not possible to directly obtain the impulse response *h(t)*. The advantage of the sweep signal though, is that its inverse

function is the signal itself inverted on the time axis and pre-equalized [40]. In case of exponential sine sweep (ESS), it must be considered that the signal's pink spectrum decreases -3 dB/octave in a Fourier spectrum (Figure 5). Therefore, the inverse filter has to compensate for this: a proper amplitude modulation must be applied to the reversed sweep signal, to make the amplitude increase +3 dB/octave, as shown in Figure 6, and get a flat output spectrum.

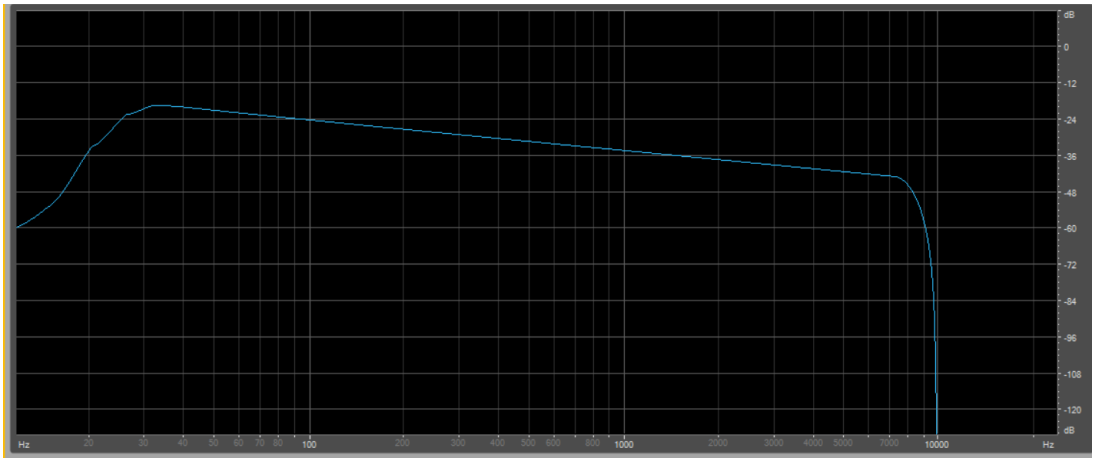

Figure 5: Exponential Sine Sweep's pink spectrum, which decreases 3 dB per octave.

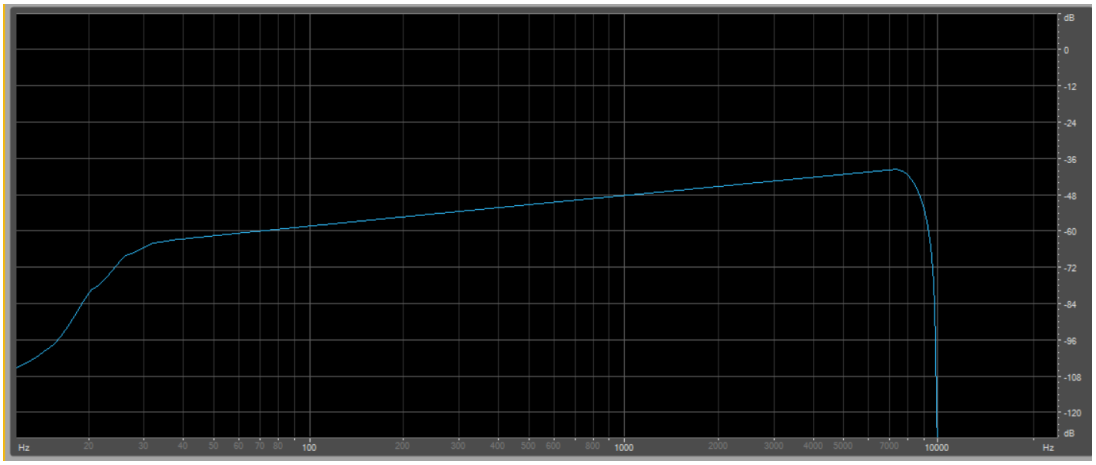

Figure 6: Inverse sweep signal, modulated to increase 3 dB per octave.

This means that the deconvolution corresponds to a convolution of these two functions, that produces a Dirac's delta function $\delta(t)$, which has a flat spectrum (Figure 7).

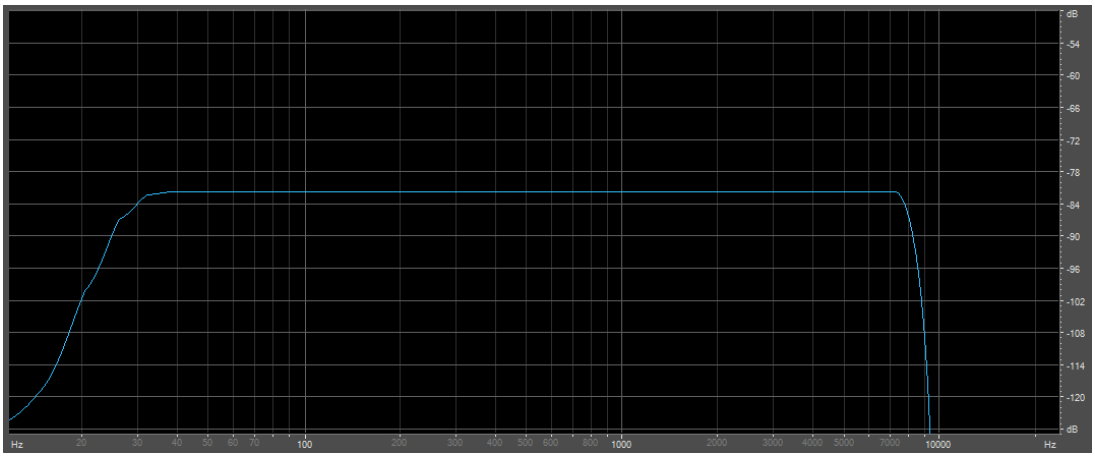

Figure 7: Dirac' delta flat spectrum.

The ESS presents some advantages compared to the linear one:

1. A better energy distribution over the spectrum: an exponential sine sweep has higher energetic level at low frequency, thanks to the slow initial growth rate, giving a pink spectrum (versus the white spectrum of a linear sweep).
2. A better signal to noise (S/N) ratio
3. It is possible to study the system's distortion. In case of harmonic distortion, the system generates an output with harmonics' presence. In the invers filter convolution problem, the impulse responses due to the distortions are at the linear IR's left. In case of linear sweep (Figure 8 and Figure 10), the undesired responses are messily distributed (the distance between consequent harmonics varies on the time axis), while with an ESS this doesn't occur (Figure 9 and Figure 11). In fact, the logarithmic feature of the frequency axis makes the time advance "packing" of every harmonic order constant, so the impulse responses of the frequencies produced by the distortion are well detached. Hence, applying a suitable time window, it is possible to isolate the linear response and discard the distortion products.

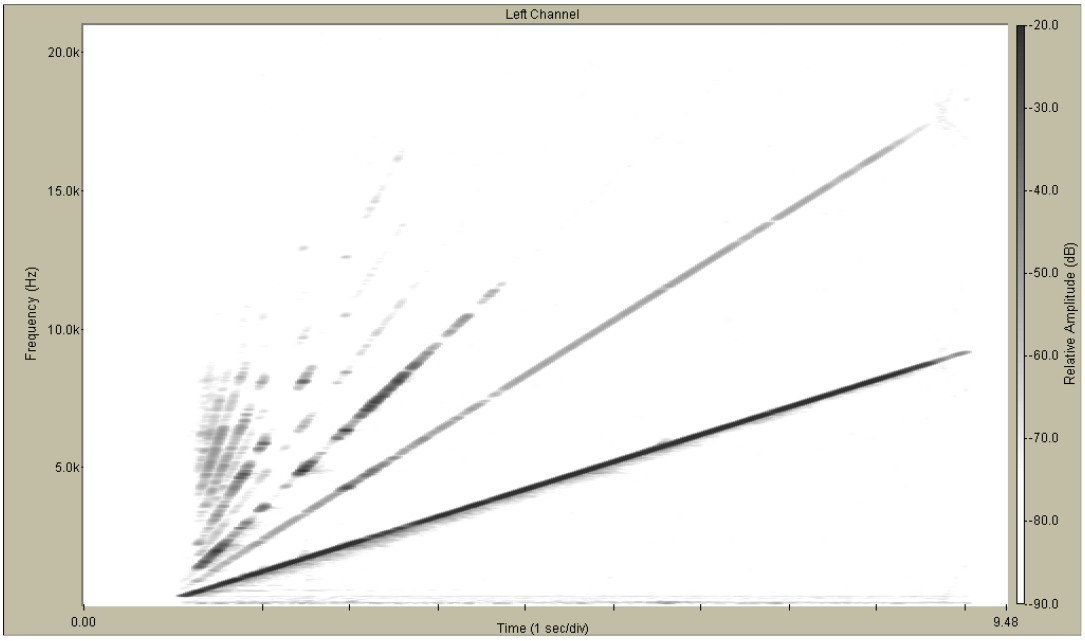

Figure 8: Output of a measurement with linear sine sweep. Blurry lines are due to the system's distortion, which generates a series of harmonics.

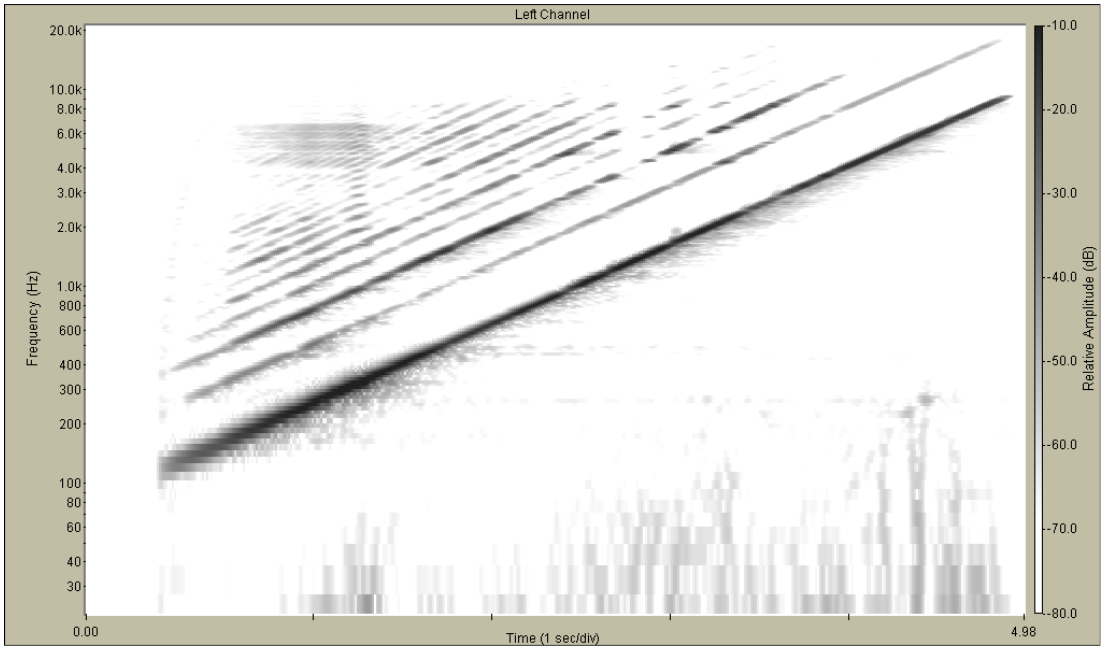

Figure 9: Output of a measurement with exponential sine sweep. Blurry lines are due to the system's distortion, which generates a series of harmonics. Here their impulse responses are well detached though.

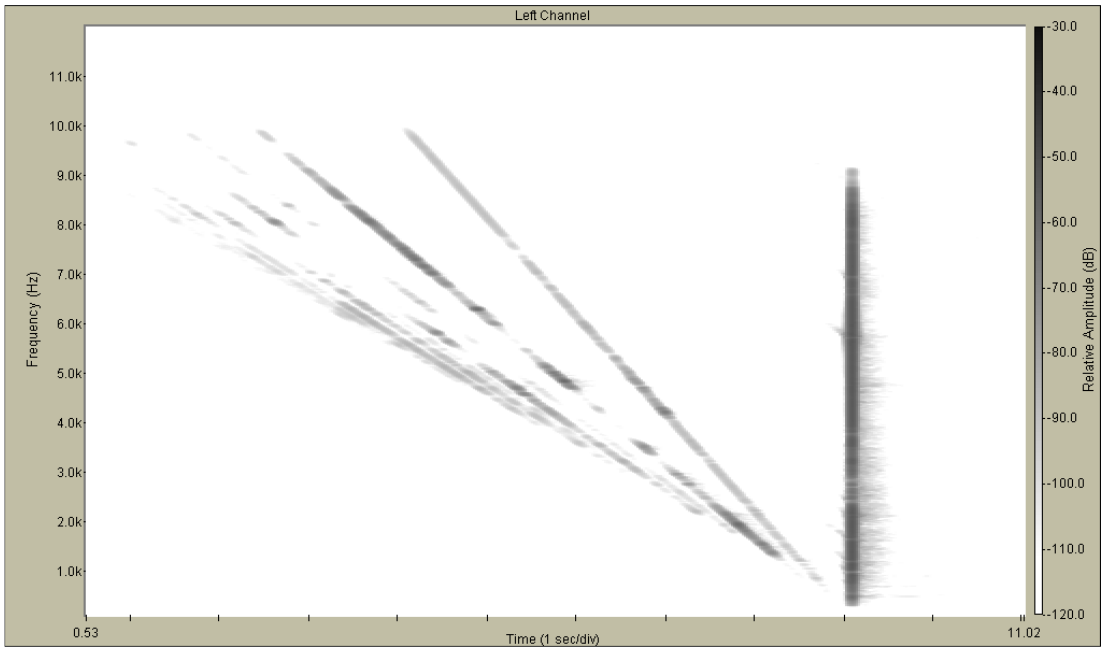

Figure 10: Impulse response obtained from linear sweep. The linear response of the system is the vertical line at the very right of the chart.

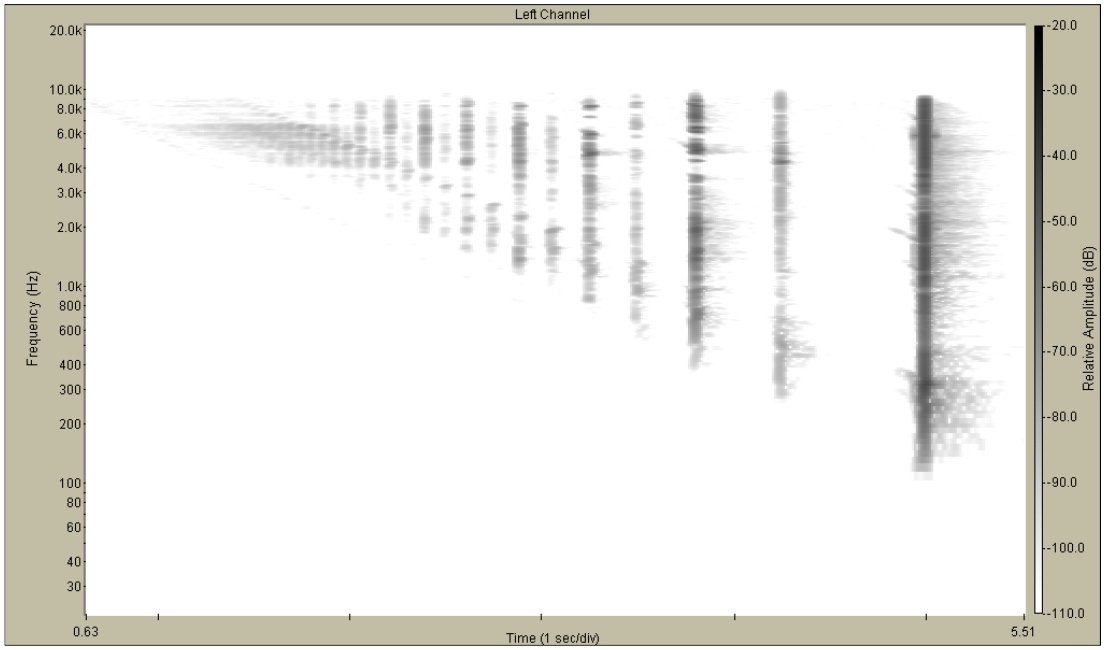

Figure 11. Impulse response obtained from exponential sweep. The linear response of the system is the vertical line at the very right of the chart.

2.5.3. ESS Related Problems

Despite the considerable advantages of the ESS method, some issues can still be found [41]. The measured IR often shows significant pre-ringing. This is demonstrated directly performing the deconvolution of the impulse response on the original test signal, without transmission through the device under test

(DUT). Doing so, one should get an ideal Dirac's delta function. Figure 12 shows what happens instead.

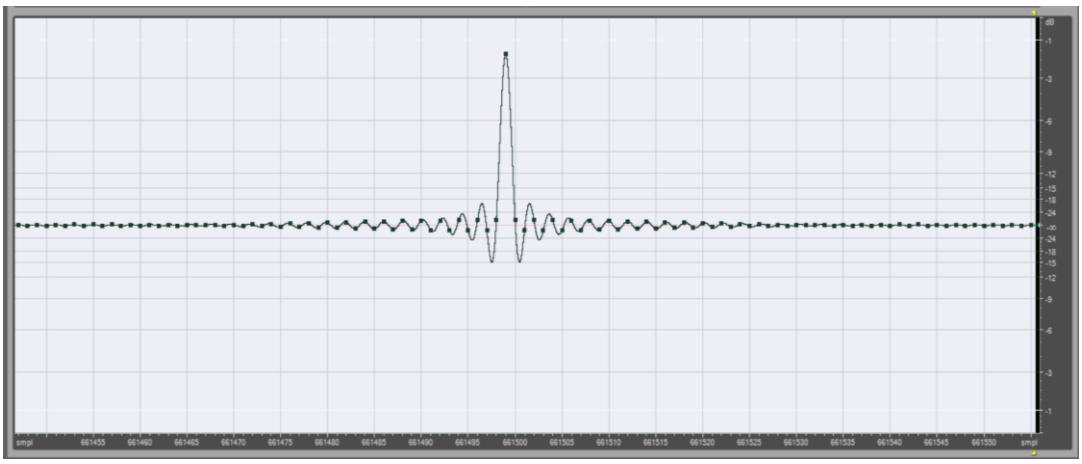

Figure 12: pre-ringing artifact with fade-out.

A series of damped oscillations before and after the main peak appear. This is caused by the signal's limited bandwidth (22 Hz to 22 kHz here, since the audio band for human hearing system lays in these limits) and by the presence of some fade-in and fade-out on the test signal, needed to create a smoother windowing of the signal (0.1 s in this case, employing a 15 s long ESS). However, the situation improves significantly removing the fade-out (Figure 13).

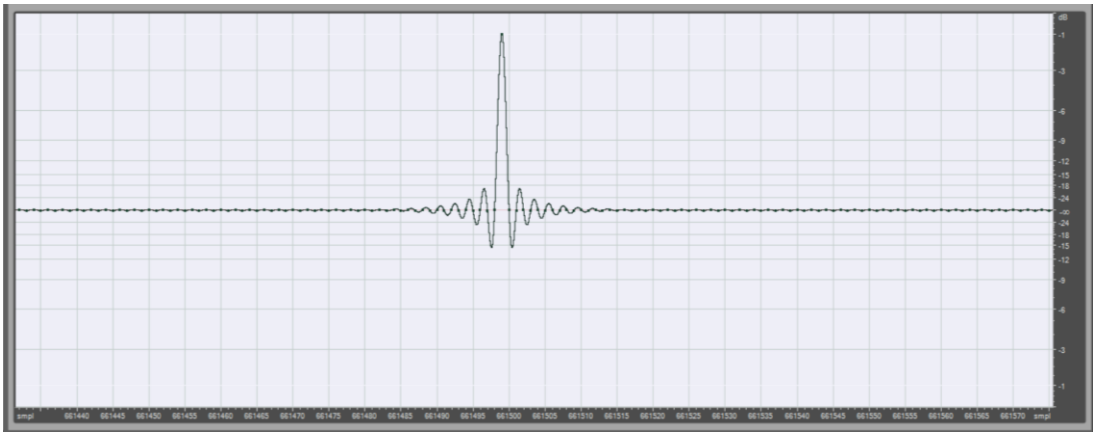

Figure 13: reduced pre-ringing artifact without fade-out.

Although, completely removing the fade-out is not the best solution: at the end of the sweep, the computed final value could be not-zero, consequently the sound system would be excited by a step function (thus spreading a lot of energy along the spectrum). Instead of deleting the fade-out, the sweep can be extended up to

the Nyquist frequency (24 kHz for the current standard sampling rate, that is 48 kHz), and cut manually in correspondence of the latest zero-crossing before its sudden termination. In this way, no pulsive sound is created and the full-bandwidth of the sweep avoids almost completely the high-frequency pre-ringing [41].

2.6. Kirkeby's Inversion Method

When taking acoustic measurements, the sound source properties heavily affect the results. A single loudspeaker, for example, is not capable of reproducing the whole audible frequency spectrum, for it depends strongly on the transducer's dimensions. Moreover, its performance might not be equal (flat) at all frequencies, causing an intrinsic flaw in the measurement chain. There are cases where a post process of signals is not a big issue, but in other situations it is preferable to pre equalize the spectrum in order to compensate the transducer's lacks. If one wants to study the response of a vibro-acoustic radiator, it has to be taken into account that the performance will be affected also by the one of the exciter. Hence, when analyzing its frequency response function, it must be considered that the measured data do not depend only on the vibrating structure's properties and boundary conditions. An equalization procedure has to be performed, which means a filter needs to be applied to the spectrum. To do so, a finite impulse response (FIR) filter has to be synthetized [42] and, in this case, it basically consists on the inversion of the measured sound pressure curve in function of frequency to "shape" it as one needs. Direct inversion of the signal is often not admitted though. Therefore, different approximate inversion techniques have been created, but in this work the Kirkeby's method for single-input single-output (SISO) systems is considered [41], [43]. His technique expects to calculate the inverse in frequency domain, adding a frequency dependent regularization parameter $\varepsilon(\omega)$ [43]. The algorithm can be summarized as follows:

1) The IR to be inverted is transformed by Fast Fourier Transform (FFT) to frequency domain:

$$H(\omega) = \int_{-\infty}^{+\infty} h(t)e^{-j\omega t}dt$$

Eq. 30

2) The computation of the inverse filter $C(\omega)$ is processed as:

$$C(\omega) = \frac{Conj[H(\omega)]}{Conj[H(\omega)]H(\omega)\varepsilon(\omega)}$$

Eq. 31

3) The filter is inverted back to time domain.

The frequency dependence of the regularization parameter avoids it to exceed the signal's frequency band. Furthermore, in correspondence of the extreme bands $\varepsilon(\omega)$ has usually a much higher value than at the spectrum's centre, where it is set very small to have an accurate inversion (Figure 14). The regularization parameter's value is calculated through a trial-and-error approach, finding a compromise between the filter's length and the thorough inversion of peaks and valleys, together with its accuracy. This is because it's hard to define an optimum value for the whole frequency band.

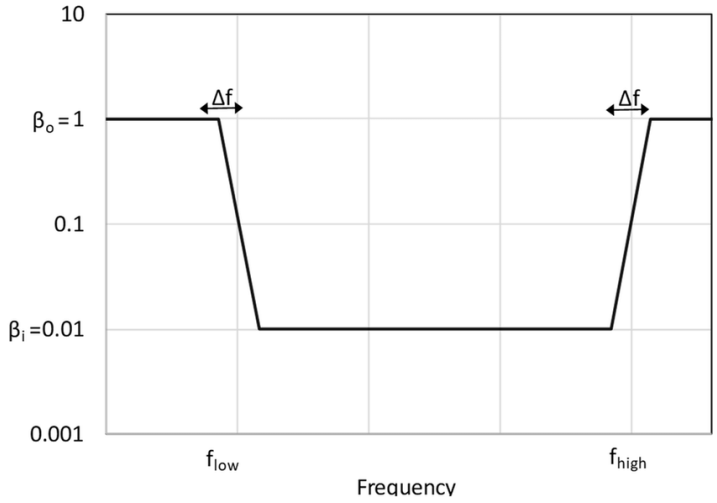

Figure 14: Frequency trend of the regularization parameter. $\varepsilon(\omega)$ has a much higher value than at the spectrum's centre, where it is set very small to have an accurate inversion.

3. Analytical and Numerical Models of Sound Radiated by Isotropic Rectangular Plates

When a complex model or solution must be developed, a good preliminary step is to create, test and validate a simplified one. In this case, the final purpose of creating a vibro-acoustic sound enhancement system based on vibrating panels, led to the preparatory study of flat panels' behavior when excited by vibrating transducers. The aim was to have both an analytical and a numerical model that could predict the sound radiated by vibrating flat (or just shallow) surfaces. Their project and evolution are here explained.

3.1. Analytical Model

The first model was developed in Matlab employing the analytical solution of the motion equation of rectangular isotropic fully clamped undamped plates under harmonic excitation. The combination with Rayleigh's integral allowed the acoustic radiation study and prediction. In fact, as described in the previous section, Rayleigh's approximation exploits the velocity of each monopole that contributes to the sound pressure generation, i.e. of every point of the surface whose velocity is known. Therefore, the algorithm solves the motion equation following the procedure exposed in paragraph 2.3 and can be summarized as follows:

1. A rectangular plate is generated choosing ad lib its geometrical dimensions (length, width, and thickness). The plate's material is defined assigning its

mechanical properties (density, Poisson's ratio, Young's modulus), keeping into account that the solution is calculated for isotropic materials, undamped.

2. The acoustic medium properties are assigned (density and speed of sound in it).
3. The applied force intensity and position are set (it acts in normal direction).
4. The frequency band to be considered is chosen and the frequency resolution is consequently defined.
5. The plate gets discretized by a rectangular grid with a mesh resolution Δs, which must have at least 6 points per wavelength to provide a correct solution [44] (Figure 15). The grid's nodes are the points where the solution of the motion equation is calculated. To speed up the process, the solution doesn't get calculated at the borders' nodes, since they respect the fully clamped condition, i.e. they don't vibrate.

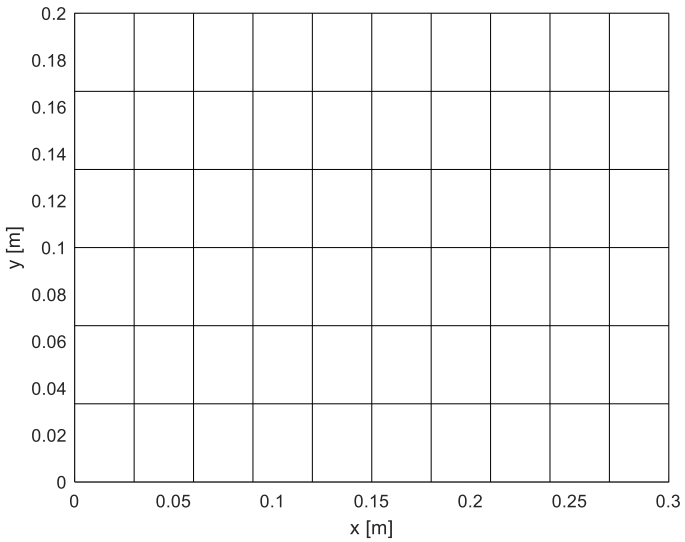

Figure 15. Example of plate discretization with a rectangular grid generated in Matlab. In this case a 300 mm by 200 mm by 1 mm plate is depicted, with a 30 mm resolution grid.

6. The node's displacement matrix in the normal direction (caused by the application of the harmonic force) is calculated all over the selected frequency band (Figure 16).
7. The displacement matrix is derived to get the normal velocity one, to calculate Rayleigh's integral inputs.

8. Rayleigh's monopole approximation is calculated, obtaining the acoustic pressure matrix at the evaluation point.
9. The generated SPL is consequently determined at arbitrary distance (usually 0.5 m or 1 m on axis). The accumulated acceleration level is calculated too (AAL, see Section 2.4).
10. A-weighting is performed.

An aluminium plate with dimensions a = 0.3 m, b = 0.2 m, and h = 1 mm (respectively length, width, and thickness) is considered as example. The mechanical properties are $\rho = 2710 \frac{kg}{m^3}$, $\nu = 0.33$ and $E = 70\ GPa$. The frequency range is set between $f_{min} = 150\ Hz$ and $f_{max} = 1\ kHz$. The magnitude of the exciting force is $F = 1\ N$. Air properties are the following: $\rho_{air} = 1.2 \frac{kg}{m^3}$ and $c = 343 \frac{m}{s}$. The minimum mesh resolution to be adopted can be obtained with the following simple formula:

$$\Delta s = \frac{\frac{c}{f_{max}}}{6}$$

Eq. 32

In this case, the resolution would be 0.057 m as maximum value, meaning that it's the minimum resolution that would provide correct results at 1 kHz. To have a better result, Δs is set at 0.03 m.

If, for example, the point force is applied at the plate's center, the deformation patterns in the normal direction (which will be referred as z-direction) caused by the forced vibration assume the shapes depicted in the Matlab plots of Figure 16, where they are reported from 100 to 1000 Hz, every hundred hertz. The surface plots are obtained with a frequency resolution of 1 Hz.

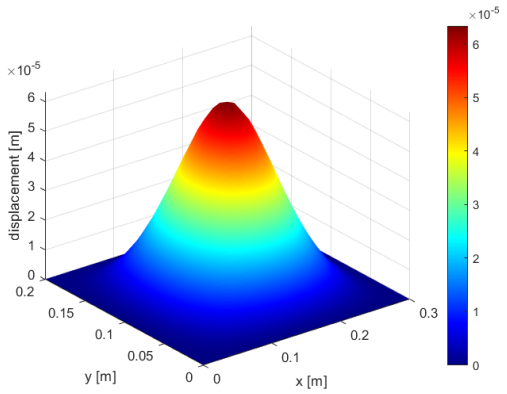
displacement [m]
y [m]
x [m]

a)

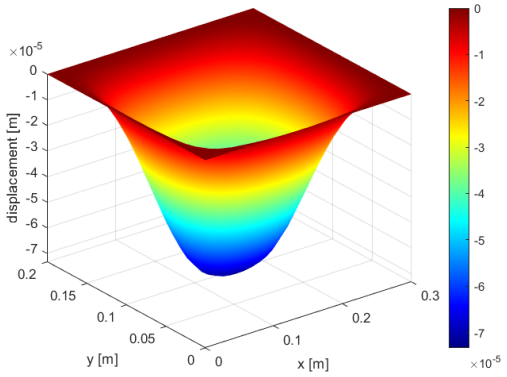
displacement [m]
y [m]
x [m]

b)

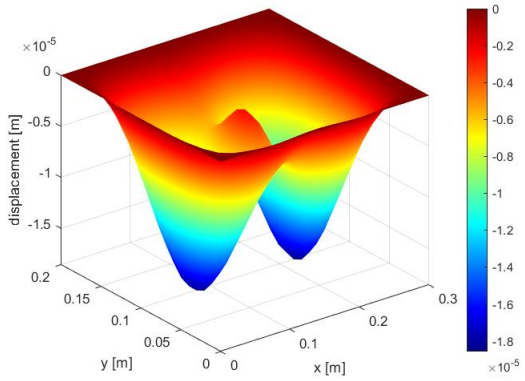
displacement [m]
y [m]
x [m]

c)

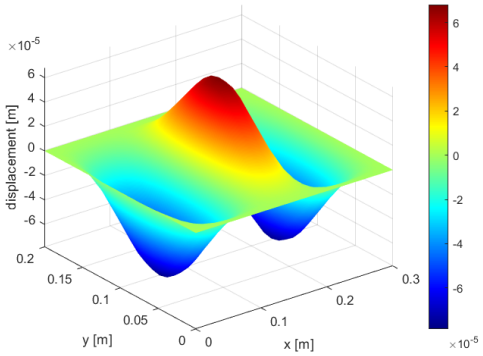
displacement [m]
y [m]
x [m]

d)

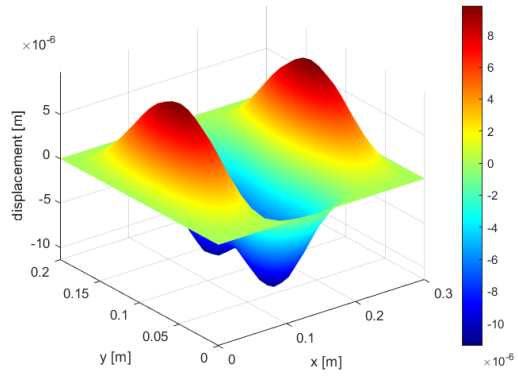
displacement [m]
y [m]
x [m]

e)

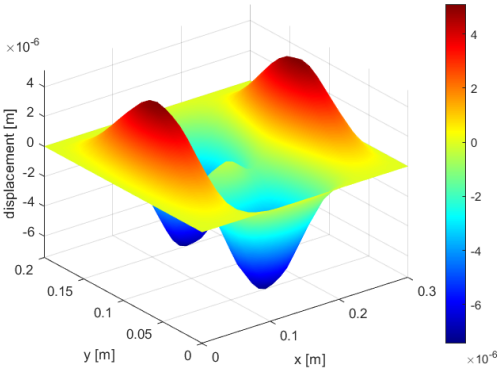
displacement [m]
y [m]
x [m]

f)

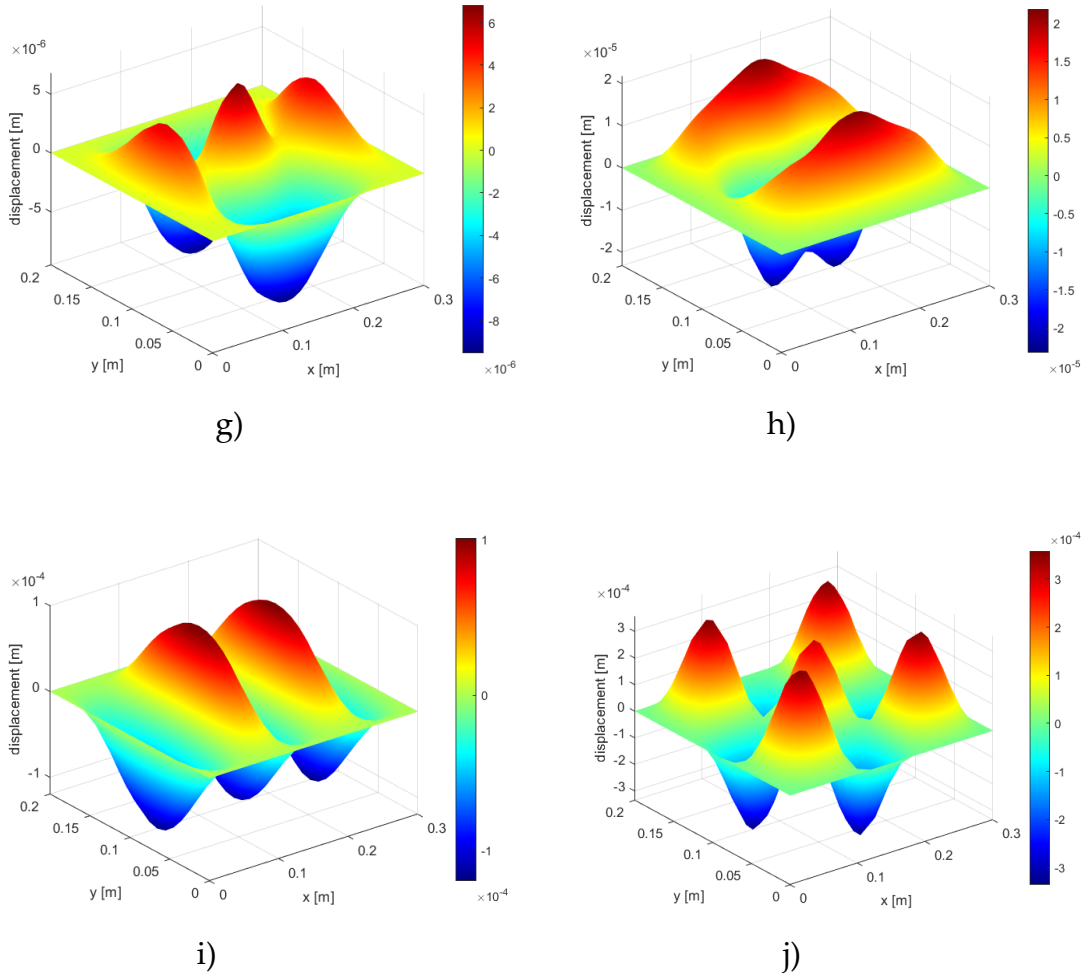

Figure 16: Deformation Matlab plots in normal direction to the plate due to harmonic excitation at its centre, with a sinusoidal force of 1 N amplitude. The patterns are shown for a) 100 Hz, b) 200 Hz, c) 300 Hz, d) 400 Hz, e) 500 Hz, f) 600 Hz, g) 700 Hz, h) 800 Hz, i) 900 Hz, j) 1000 Hz.

To perform Rayleigh's integral (which is approximated by a sum, as equation Eq. 22 showed), the discretized pumping sub-areas (the monopoles) must be calculated. They are nothing but the small rectangles defined by the mesh grid. It's important to notice one detail: the motion equation gets solved at the nodes of the grid, which lay in the middle of 4 sub-areas (visible in Figure 15), and not at their centers. Anyway, the competence surface of each node corresponds exactly to the areas determined by the grid. What's more, being the nodes on the borders fixed, their portion of (non) vibrating area is set as zero in the equation. So, deriving the z-direction displacement matrix, the normal velocity matrix is obtained. Once the evaluation position in the front space is set (for example, one

meter distance on axis from the plate's center), all the input data for Rayleigh's approximation are established.

3.1.1. Frequency Resolution Influence

If for the discretization grid a mathematically determined spatial resolution is needed to obtain correct results, the same can't be stated for the frequency resolution. In fact, it doesn't affect the validity of the motion equation solution itself, rather it determines a smoother or coarser spectrum. Furthermore, in models where the system is considered undamped, the frequency response tends to infinity in correspondence of the resonance frequencies. If the frequency resolution is too broad, this behavior won't be observed though. Figure 17 shows a comparison between sound pressure level curves at 1 meter distance, where three different frequency resolutions have been applied: smoother peaks appear along the blue curve, which has 10 Hz resolution, which are typical of damped systems, but this is just an artefact due to the bad frequency resolution. As it increases, first at 5 Hz (green curve) and then at 1 Hz (red spectrum), this phenomenon tends to disappear, and the frequency responses are more in accordance with the theoretical solution, since they sharpen, pointing to infinity.

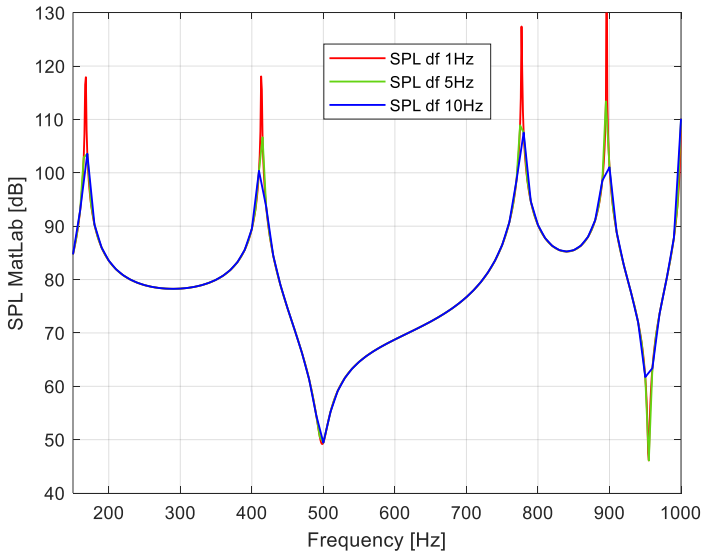

Figure 17: Sound pressure level curves at 1 m distance on axis, with 1N force applied in the centre of the plate, with three different frequency resolutions: blue 10 Hz, green 5 Hz, red 1 Hz. It is visible how a higher resolution corresponds to resonance peaks that tend to infinity, in agreement with the theoretical solution for undamped case.

3.1.2. Algorithm's Improvements

Once the fundamentals of the algorithm have been written and successfully tested, an extension of the method was produced. The main upgrades were two:

1. The evaluation of the SPL was extended to a grid of points, placed on a semi sphere concentric with the plate, and then averaged.
2. The force application point was parameterized to find the optimum one, according to specific requirements.

The 1 m on-axis evaluation of the sound pressure level is a standard approach but can lack of important spatial information. It can in fact result in misleading responses and poor realistic prediction of the generated sound field. If the listener stands in another position, which may be off axis, the phase contribution difference of the acoustic pressure can produce a very unlike perception. This is more and more true as frequency increases, due to the shorter wave lengths and consequent faster phase change. So, the idea was to solve Rayleigh's integral in the *m* points of a grid placed over a hemisphere concentric with the plate, having radius *r*, then to average the calculated sound pressures and get an average SPL curve. In Figure 18 an example of evaluation grid is reported, for a set of 81 points on a spherical surface of 1 m radius.

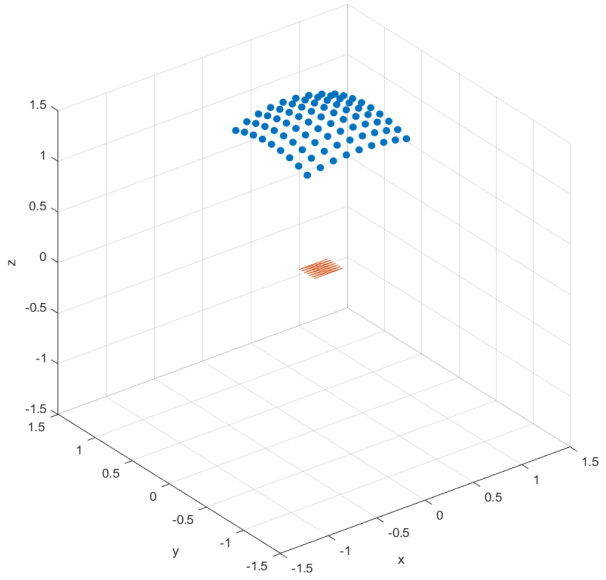

Figure 18. An example of a 81 points observation grid on a 1 meter radius semi sphere (blue dots) plotted in Matlab. The plate is highlighted in red.

The position of the exciting force can heavily affect the frequency response of vibrating panels, depending on their geometrical features (the more the plate has a complex shape, the more the phenomenon occurs). It was hence opted to investigate different force application points, in order to optimize the results. Since this operation could provide a very large number of results, being "optimum" a relative term, some optimization strategies were developed to identify the target SPL output. Moreover, due to the plate's symmetry, the code was iteratively run sweeping the force application point on the nodes of the first quadrant of the mesh (Figure 19), and not all over it.

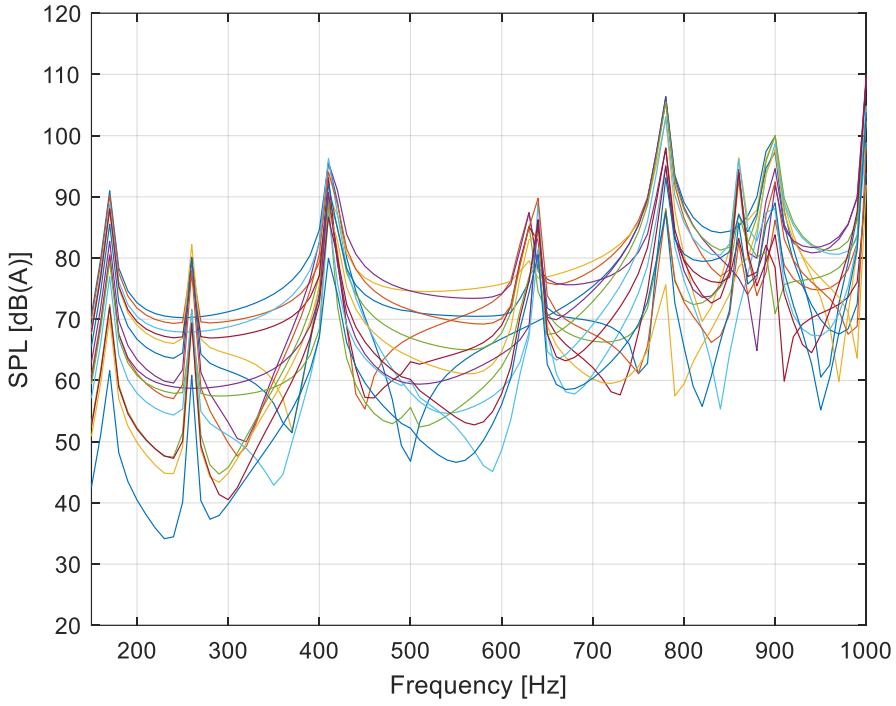

Figure 19. SPL(A) curves obtained by exciting all the free points of the first quadrant of the plate.

Two possible optimum sound pressure level curves were selected:

1. The maximum A-weighted mean SPL curve, named $SPL_{avg(A)}$, calculated with:

$$SPL_{avg(A)}(\boldsymbol{r}_{\text{obs}}) = 20log\left(\frac{\sqrt{\frac{1}{n_f}\sum_f |P(\boldsymbol{r}_{\text{obs}}, f)|^2}}{p_0}\right)$$

Eq. 33

where n_f is the number of frequencies.

2. The minimum standard deviation SPL curve.

In the first case, the target SPL curve is somehow what one could define the "loudest" in common terms. It must be noticed that it does not correspond to an equivalent level calculation (L_{eq}), which is an average over time, but to an average of pressure values along the frequency band. In the second case, the standard deviation is directly calculated over the peaks of the SPL curves. The decision of this type of target curve was taken more from an auditory quality perception point of view, since a flatter spectrum corresponds to a "smoother" listening effect (it is in fact the basis of the equalization processes). In addition, since one may prefer a certain trend compared to another, the code identifies the best 4 curves with minimum standard deviation of peaks and the user can choose the preferred one. Once this "human supervision" operation is done, the code returns where the force must be applied in order to get the selected spectrum.

3.1.3. Results

Again, an aluminum plate of dimensions a = 0.3 m, b = 0.2 m, and h = 1 mm is taken as example, with the above-mentioned mechanical properties. At first, AAL, SPL, and A-weighted SPL curves were calculated on-axis at one meter distance. In Figure 20 an example is shown for the force applied on point ($x = 0.21\ m\ ; y = 0.1\ m$). It is possible to notice the break-up occurring around 200 Hz and the acoustic cancellation that occurs above (since the piston mode displacement ends, anti-phase components of the generated air pressure appear). The consequent canceling effect is visible from the difference between AAL peaks and SPL trend). One can also notice that the resonance peaks tend to infinite, due to the absence of damping in the analytical solution.

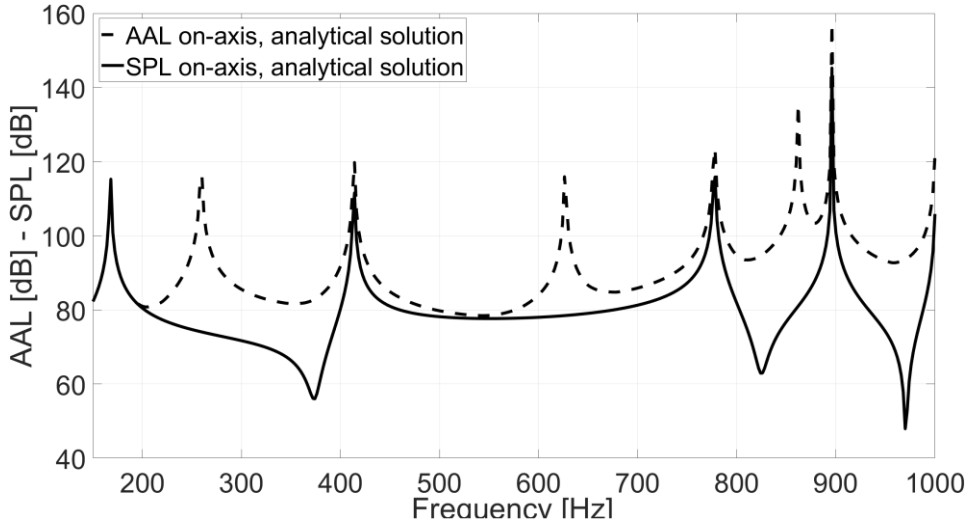

Figure 20. AAL (dash line) and SPL (solid line) curves, evaluated in a point on-axis at 1 m distance. Analytical solution, force applied in (x, y) = (0.21 m, 0.1 m).

It is clearly noticeable how space averaging can affect the results: some peaks of the AAL curve that were not present in the SPL curve of Figure 20 (calculated only in one point on-axis) are visible in the solid SPL curve of Figure 21, meaning that a less smooth listening effect would reach the audience. The average over the observation grid therefore effectively allows a more realistic evaluation of the generated soundscape.

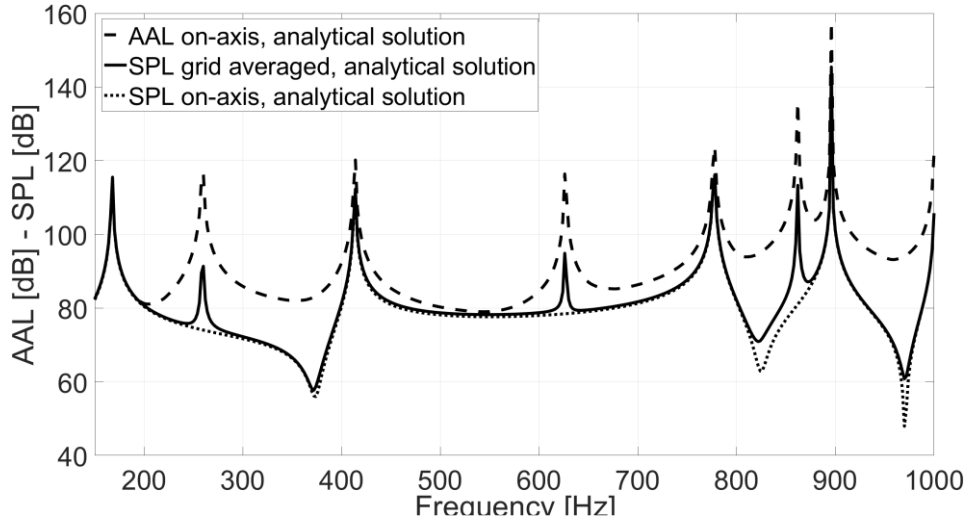

Figure 21. AAL (dash-dot line) and SPL (dot line) curves evaluated in one point on-axis at 1 m distance, and SPL (solid line) curve averaged over 45 observation points. Analytical solution, force applied in (x, y) = (0.21 m; 0.1 m).

The optimization procedure allowed to identify the optimal position of the exciting force application points according to the two selected criteria (Figure 23).

At first, the maximum *SPL_avg(A)* was obtained applying the force at the centre of the plate (green dot in Figure 22).

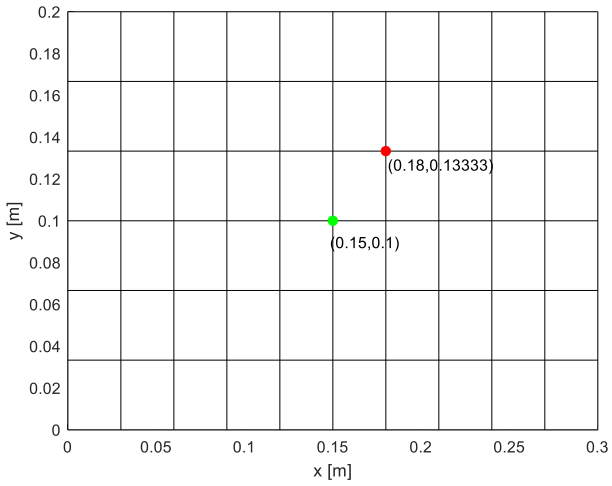

Figure 22. Optimal force application points, green for maximum $SPL\_avg(A)$ and red for flattest frequency response.

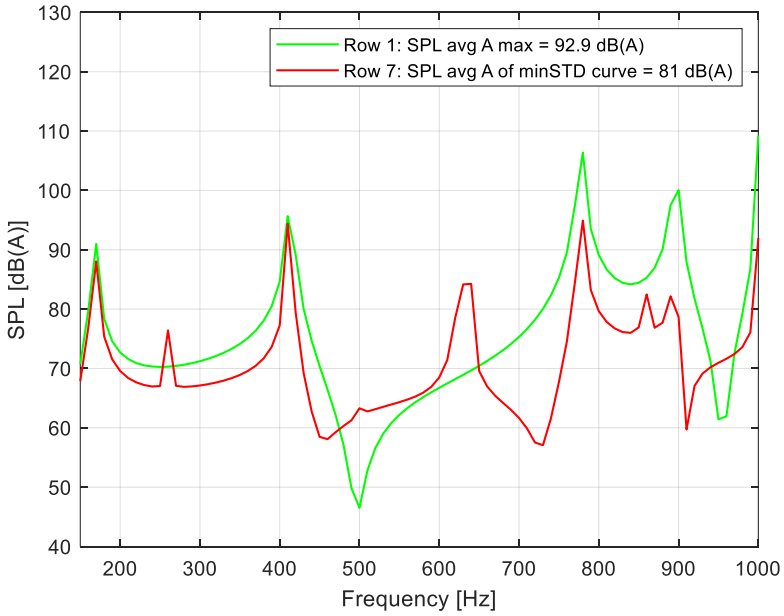

Figure 23. Maximum $SPL\_avg(A)$ for a 300mm by 200 mm by 1mm aluminium plate (green curve), and minimum standard deviation SPL curve obtained for the same plate (red curve).

The flattest spectrum instead, was sought among the best four curves with minimum standard deviation of SPL peaks of Figure 24. The best one, mathematically speaking, was obtained when the force is applied in correspondence of the red dot of Figure 22. As was previously mentioned, a human supervision contribute can establish the preferred one and the code would return where to apply the excitation source.

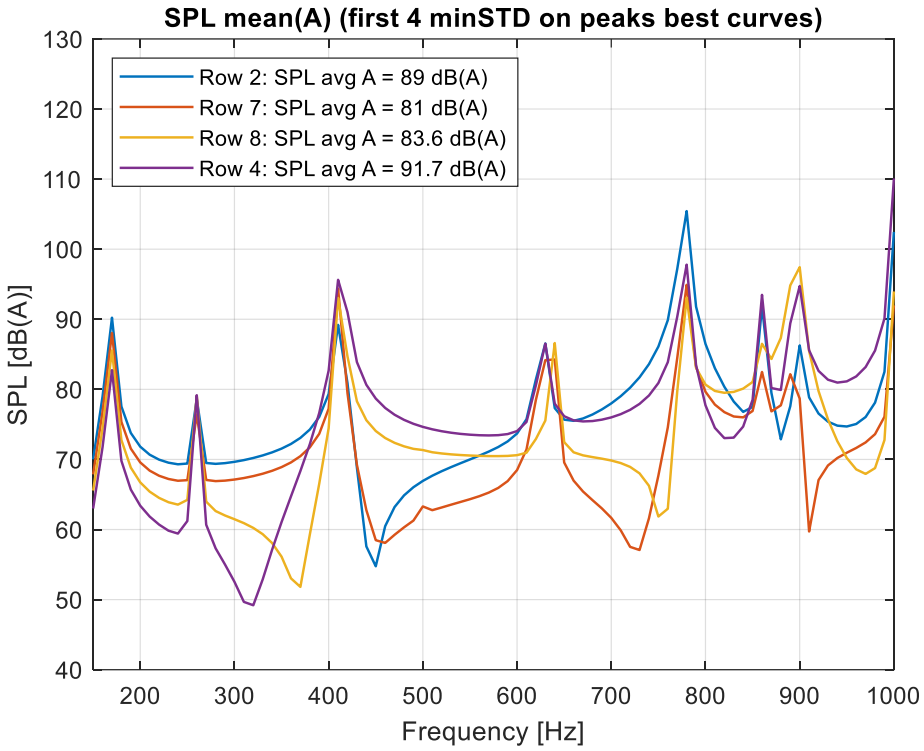

Figure 24. Matlab plot of the best four SPL curves with minimum standard deviation of peaks for a 300mm by 200mm by 1mm aluminium plate excited with a 1 N force.

3.2. Numerical Model

The numerical model was developed with COMSOL Multiphysics FEM solver. The model had to provide a solution to a vibroacoustic problem, so the plate was designed clamped in the middle of a rigid baffle (made simply through a work plane) and surrounded by an air sphere of radius variable with the chosen evaluation distance (Figure 25). The baffle splits the sphere in two parts, simulating the front and rear acoustic radiation separation, as Rayleigh's hypothesis requires. Two modules were employed, Pressure Acoustic - Frequency Domain and Solid Mechanics, linked by the Acoustic-Structure boundary coupling.

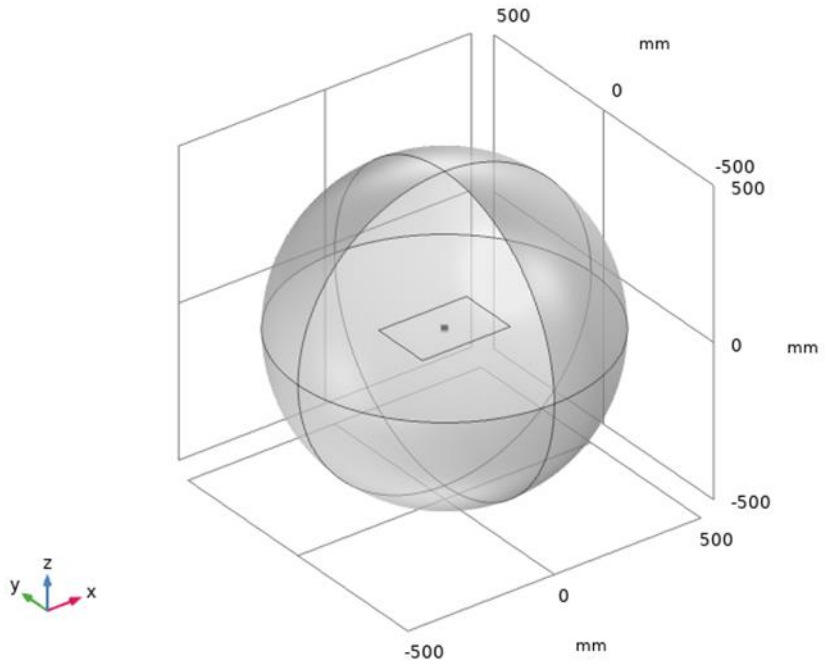

Figure 25. Comsol model of the plate fixed in a baffle that splits in two the air sphere of 0.5 m radius.

The aluminum plate and air properties were identical to the analytical solution, for a direct comparison requires the same input data. Furthermore, to have the best possible accordance between analytical and numerical models, the plate was subdivided in a rectangular mesh, namely a "mapped" mesh, having the same number and dimensions of the elements in the analytical solution (Figure 26 b). The rigid baffle was meshed with "free triangular" elements, while "free tetrahedral" elements were used for the air sphere (Figure 26 a). The baffle was defined with Comsol's feature "interior sound hard boundary" and the radiation boundary condition for the air domain was "spherical wave radiation". This last property simulates the free field condition since the outgoing waves do not get reflected from the sphere boundaries. In fact, Rayleigh's equation is valid in free field, which would not be respected if the sphere boundaries were behaving like walls. The simulation was calculated in the same frequency range and resolution of the analytical study.

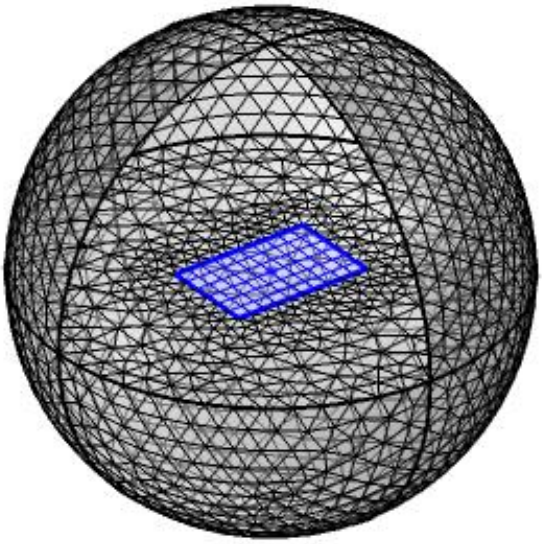

a)

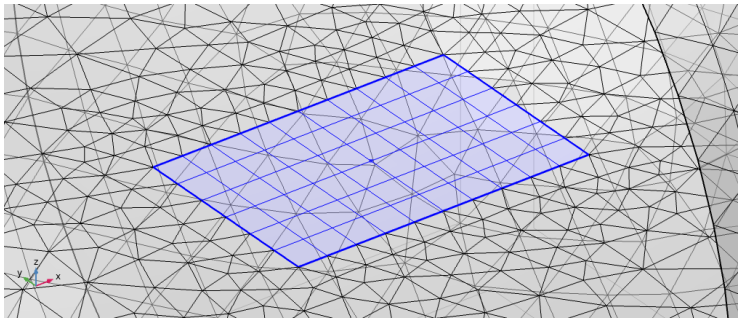

b)

Figure 26. a) Mesh of the full model and b) detail of the "mapped" mesh of the rectangular plate.

3.2.1. "Solid Structure" and "Shell" Physics

Two possible physics for the plate were available for the model: the so called "solid structure" and the "shell" physic. Their main difference is about the thickness of the element which undergoes this type of definition. In the first case, the drawing must have an effective thickness, defined at design stage. In the second case, it is established only theoretically, and the drawing is just a layer (a shell) in 2D. This means a larger number of nodes to solve in the model for the solid case, since the thickness gets meshed too. Consequently, the computational time increases, and the simulation is heavier. It was opted to verify their similarities to use the best one. An eigenfrequency study was carried out and, as Figure 27 and Figure 28 show, the discrepancy between the calculated solutions is almost irrelevant, being the gap of the eigenfrequencies (calculated in the

frequency band of interest) very little, and the modes identical. This allowed the model to be studied as a shell structure, with the further advantage of being possible to vary the plate thickness without need to redraw the geometry.

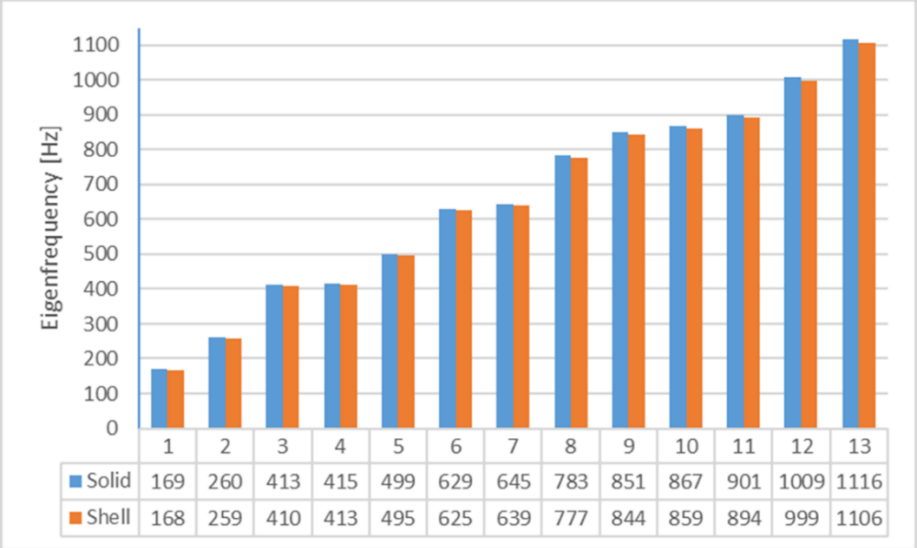

	1	2	3	4	5	6	7	8	9	10	11	12	13
Solid	169	260	413	415	499	629	645	783	851	867	901	1009	1116
Shell	168	259	410	413	495	625	639	777	844	859	894	999	1106

Figure 27. Display of the discrepancy in the eigenfrequencies values of the numerical study. Shell and solid structures return very similar results.

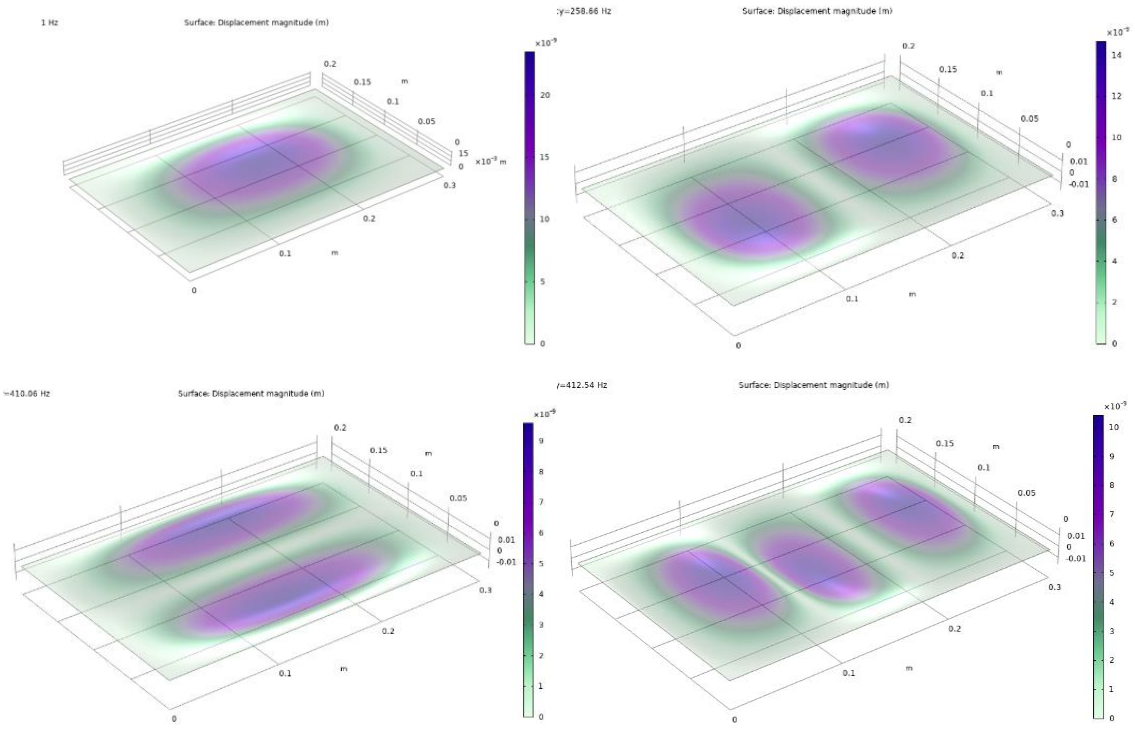

a)

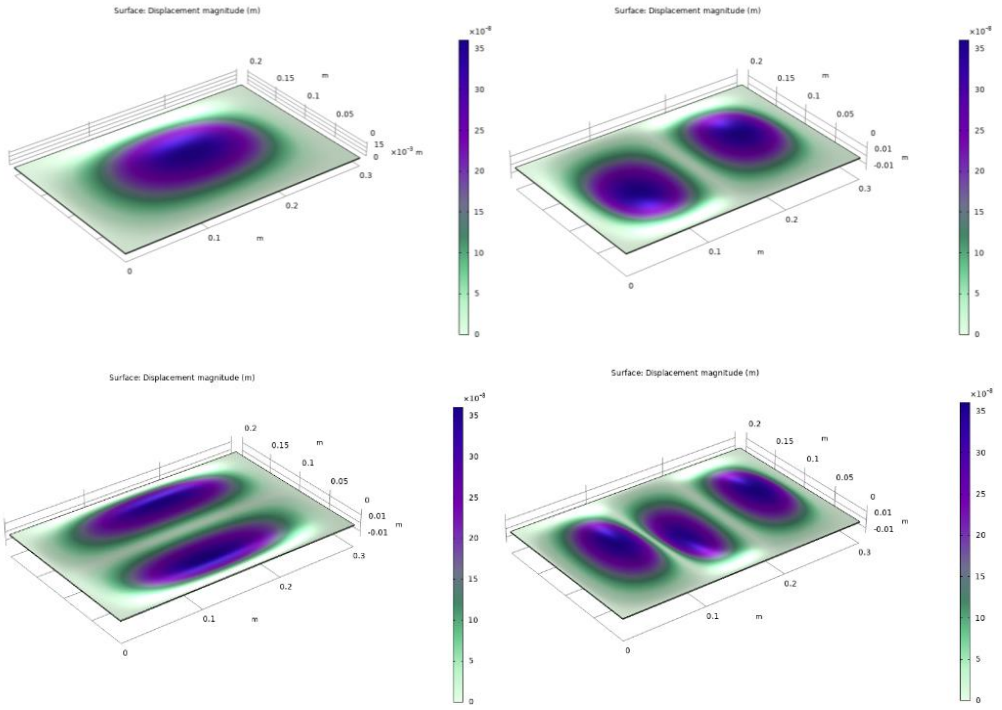

b)

Figure 28. First four modes of the eigenfrequencies study carried out in Comsol for a) shell and b) solid physics.

3.2.2. Results processing

The sound pressure level was evaluated both in a single point on axis with the plate's centre and on a grid of points concentric with the plate (Figure 29). As for the analytical model, the extracted acoustic pressure values were then averaged and converted to an average SPL curve. This specific process was carried out in Matlab, after extracting the Comsol pressure data. In the numerical model too, the parameterization of the force application point was conducted, exploiting the "parametric sweep" function. The matrix of the obtained solutions was then elaborated in Matlab to obtain the same procedure of the analytical model, but with numerical inputs.

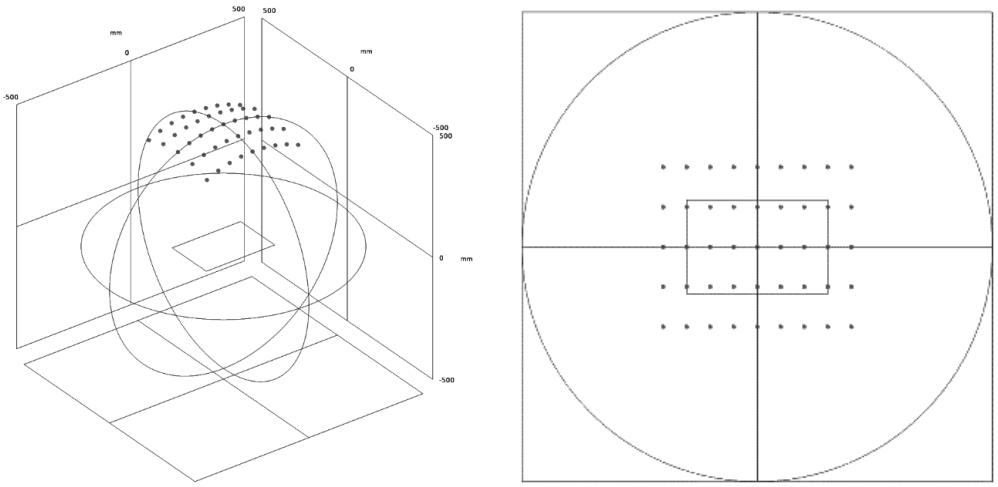

a) b)

Figure 29. a) Observation grid reported in Comsol's model; b) View of the observation grid from above.

Eventually, a numerical simulation was performed by introducing damping as an isotropic loss factor $\eta = 0.05$. In Figure 30 it is possible to see the comparison between damped and undamped cases, for a force of 1 N applied at point ($x = 0.21\ m$; $y = 0.1\ m$) and evaluated at the observation grid. One can note the effect of damping in correspondence of the resonance frequencies, where the peaks are smoothed instead of going to infinite, as it happens in real systems.

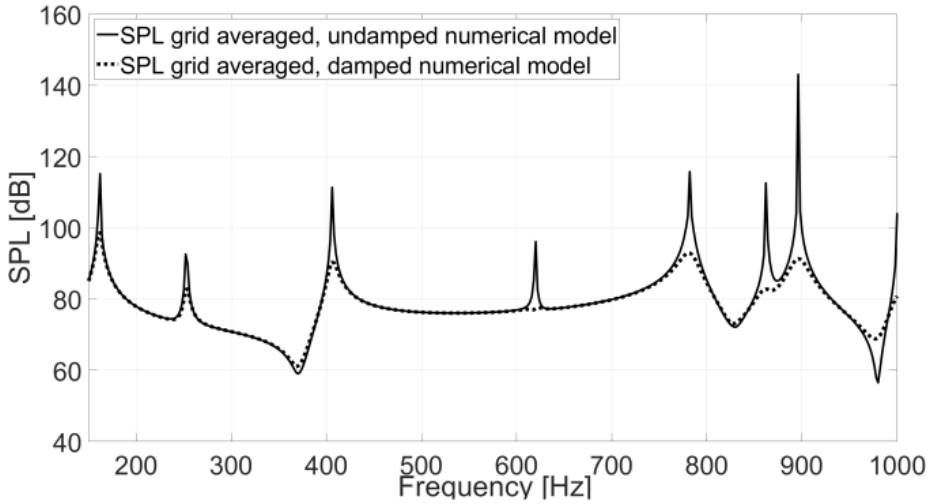

Figure 30. Superimposition of SPL curves obtained for undamped case (solid line) and damped one (dash line). Damping was introduced as an isotropic loss factor.

3.3. Results Comparison

The results obtained by the analytical and numerical models were compared to be validated. In Figure 31 the result is shown superimposing numerical and analytical SPL outputs, calculated for a 1 N force applied at the center of the plate and then averaging the acoustic pressure data over a grid of 45 observation points, at 1 meter distance. In both methods, this resulted to be the best application point of the force to maximize the *SPL_avg(A)*. Both the SPL(A) curves' trend and the values of *SPL_avg(A)* are well matched: in fact, $SPL\_avg(A)$ = 90.8 $dB(A)$ was obtained from the analytical method and $SPL\_avg(A)$ = 90.7 $dB(A)$ resulted from the numerical method, without damping and with 5 Hz frequency resolution.

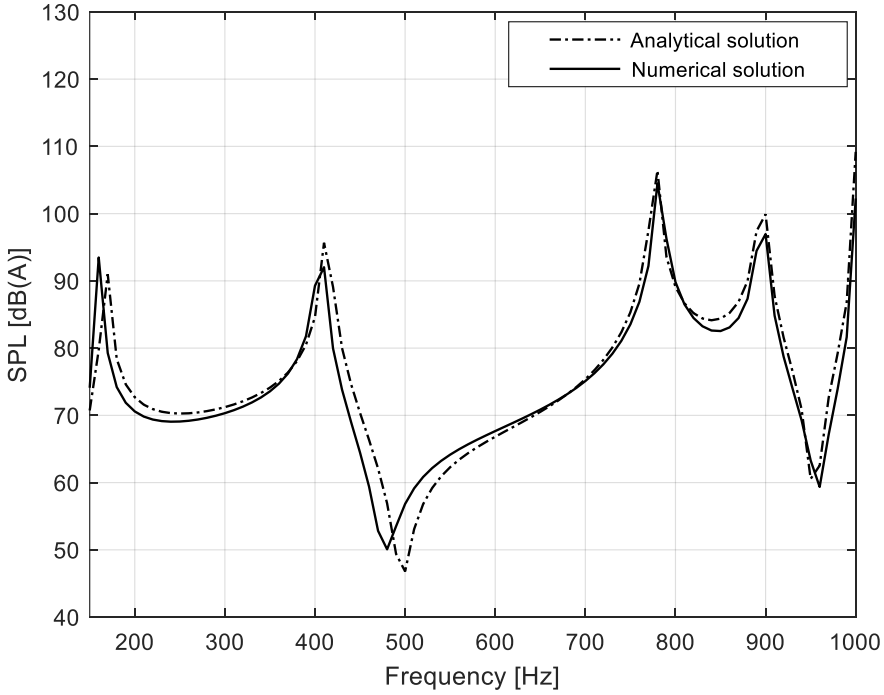

Figure 31. SPL(A) curves averaged over 45 observation points, maximum A-weighted Sound Pressure Level, analytical (dash-dot line) and numerical (solid line) solutions.

For what concerns the optimization of the force application position to get the flattest spectrum, the superimposition of the two models' results is shown in Figure 32, again averaging the acoustic pressure over the same 45 observation points (Figure 32 a). Post processing the extracted data from Comsol, the code returned the same matrix index of the force positioning coordinates (Figure 32

b). It is possible to see in the chart how also in this case a very good agreement between the two solutions was reached: both the curves and the $SPL\_avg(A)$ values are well matched, with $SPL\_avg(A)$ = 80.7 $dB(A)$ obtained from the analytical method and $SPL\_avg(A)$ = 79.1 $dB(A)$ from the numerical method. One can note that the price for having a flatter spectrum is a reduction in terms of $SPL\_avg(A)$ of about 11 dB(A), compared to the maximum sound pressure level approach.

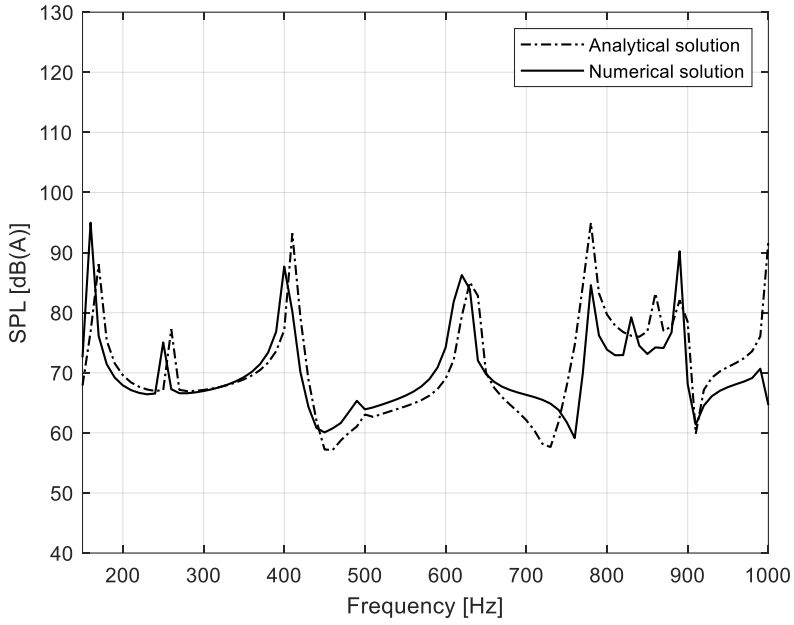

a)

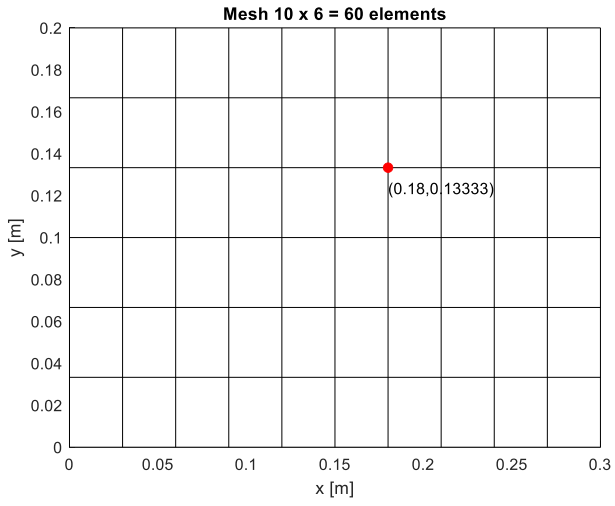

b)

Figure 32. a) SPL(A) curves averaged over 45 observation points, flattest spectrum, analytical (dash-dot line) and numerical (solid line) solutions, b) Matlab plot of the returned application point needed to obtain the depicted curves in both models.

Figure 33 shows the residual curves obtained by subtracting the SPL curves calculated by the two methods. The solutions were computed in both cases by exciting all the free points in the first quadrant of the mesh, which are 15 with the chosen discretization, and averaging each result over the grid of 45 observation points at 1 m distance. One can note that all the residual curves are in the range ± 2.5 dB. The peaks in the residual curves correspond to the theoretically undamped resonance frequencies.

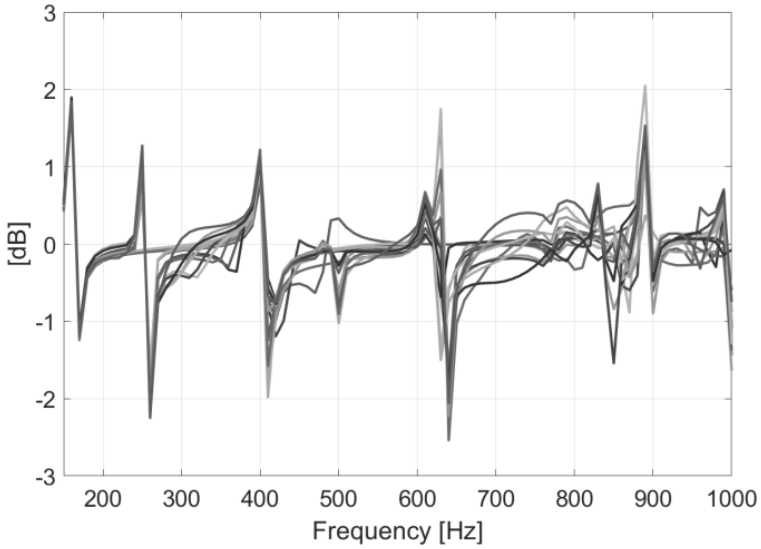

Figure 33. SPL curves averaged over 45 observation points, residual of the difference between analytical and numerical solutions. Force applied in all free points of first quadrant.

3.4. Models' Validation Through Laboratory Measurements

To have a full validation of the models, a set of laboratory measurements was conducted at the Acoustics Laboratory of the Department of Engineering and Architecture at University of Parma, Italy [45]. An aluminium alloy plate of 300 mm by 200 mm and thickness 1 mm was fixed in the middle of a plywood structure (baffle of Figure 34). A Bruel&Kjaer (B&K) shaker type 4810 was used to excite the plate and a load cell PCB 208C02 with 11241 mV/kN sensitivity was screwed on it. The shaker was placed under the plate, rigidly connected to it by a stinger (Figure 35). Such mounting of the load cell aimed to avoid any preload on the plate. To easily replicate the experimental setup in the models as closely as possible, the shaker was positioned at the centre of the panel. The

measurements were acquired with a high precision tool as the laser vibrometer [35], [46]–[48], [49] (a single point laser doppler vibrometer by Polytec), with processing unit OFV-5000 and sensor head OFV 505. The processing unit was equipped with an analogue velocity decoder type VD-01, which was set to provide a measurement range of 25 mm/s/V, with a full-scale output peak of 0.25 m/s (at the maximum output voltage of 10 V_{peak}). In this configuration, the maximum frequency was limited to 50 kHz, and a built-in low-pass filter at 20 kHz was activated. It was possible to move the sensor head with a two-axis handling system with stepping motors, controlled via laptop computer through ethernet connection and a dedicated electronic board (Figure 36). The mechanical cross talk, that is the vibration transmitted to the laser sensor head through the solid path (ground, table, handling system) was previously evaluated[35], showing a minimum attenuation of -55 dB below 1 kHz, therefore ensuring a satisfactory structural decoupling between the support and the measurement system.

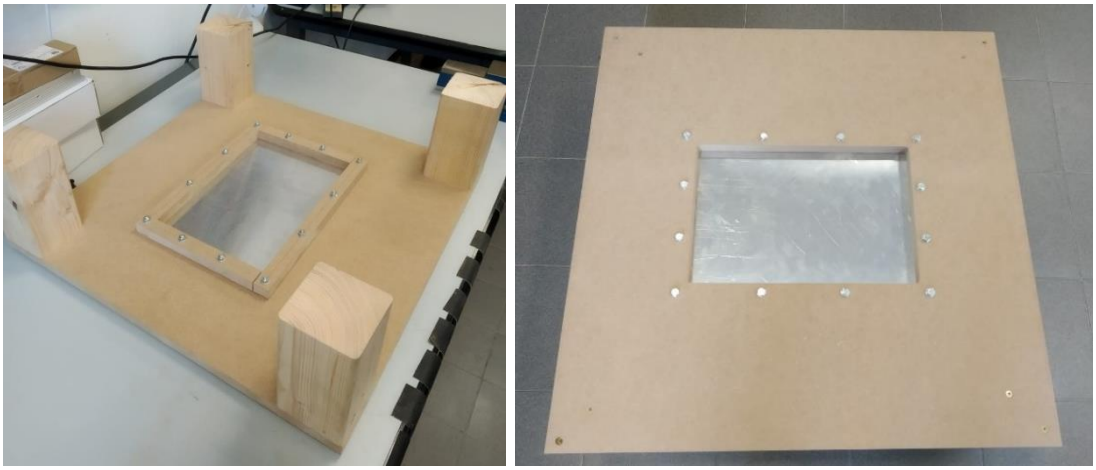

Figure 34. Aluminium plate of 300 mm by 200 mm and thickness 1mm fixed in the middle of the plywood structure adopted for the laboratory measurements.

Figure 35. B&K shaker type 4810, connected to the plate via stinger. The PCB load cell is visible at the top of the shaker.

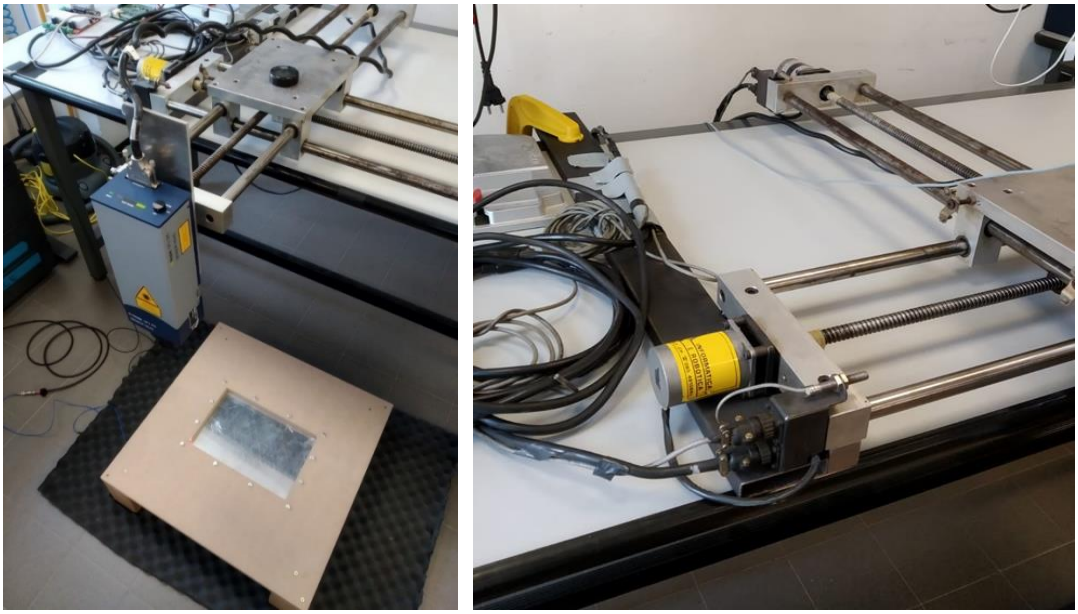

a) b)

Figure 36. a) Polytec laser sensor head and fully clamped aluminium plate mounted on rigid baffle; b) detail of the bi-axial handling system with stepping motors.

An USB audio interface (Zoom F8) was employed to manage all input and output signals synchronously (Figure 37). It was connected to the PC via USB and operating at a sampling frequency of 48 kHz. The test signal was an ESS of 10 s, played through the first output channel (a block diagram of the system is depicted in Figure 38). The signal was amplified before feeding the shaker at a voltage of 1 Volt, measured with a true-RMS meter. While playing the ESS, three

input signals were recorded by the soundcard: force from the load cell, sound pressure from a B&K measurement microphone and velocity from the LDV. Considering the target application, the frequency range of interest was comprised between 150 Hz and 1 kHz. Therefore, an ESS from 20 Hz to 2 kHz was employed, for accounting a smooth fade-in and fade-out of 0.5 s, respectively.

Figure 37. Polytec laser decoder and Zoom F8n audio card.

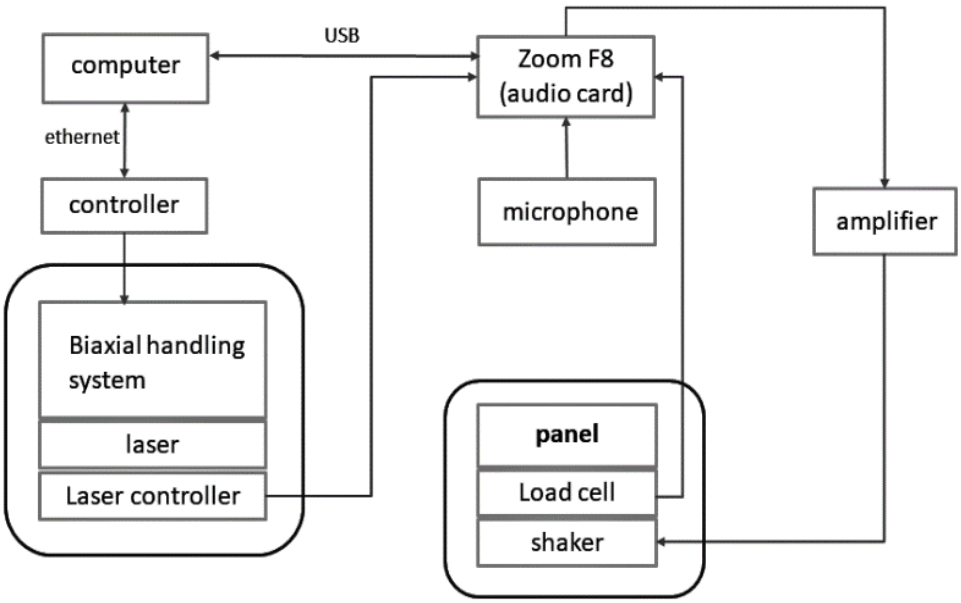

Figure 38. Block diagram of the experimental measurement system.

The acquisition system was fully calibrated before performing the measurement, so that the results could be directly compared with simulations. The rated calibration value of 11.2 mV/N was employed for the load cell. A B&K calibration system for accelerometers type 4294 was placed under the sensor head and measured for 20 s, to calibrate the laser. It produces a pure tone at 159.2 Hz with a velocity of 10 mm/s (140 dB re 1 nm/s). For the shaker calibration, a pure tone at 159.2 Hz was played through it at 1 V, and a 20 s recording of the vibrating plate was taken with the laser. A Matlab code was employed to generate the scanning grid and perform the whole measurement. A regular squared grid with a resolution of 30 mm was created, resulting in a total number of $N = 77$ points, for a measurement time of 20' (5 s of stabilization delay were employed after every movement of the sensor head). A reference acoustic measurement of the plate was acquired too, by positioning a B&K microphone type 4188 with pre-amplifier type 2186 above the plate, on-axis respect to its centre, at the standard distance of 1 meter (Figure 39). The B&K microphone was calibrated with a B&K calibration system type 4231, which produces a pure tone at 1 kHz having an RMS value of 1 Pa (a SPL of 94 dB re 20 μPa). Such measurement was used to compare the recorded output to the SPL reconstructed through Rayleigh's integral.

Figure 39. Detail of the B&K microphone mounted over the plate on-axis at 1 meter distance.

At first, the measured data were processed by means of the convolution between recorded ESS and inverse ESS, obtaining the time domain Impulse Responses (IRs) of the system. The linear part of the IRs was cut in time domain and converted to frequency domain by applying an FFT. Doing so, the spectrum of sound pressure was obtained for the acoustics reference measurement performed with the B&K microphone on-axis at 1 m distance. The velocity spectrum in each of the N = 77 points measured by the LDV was obtained too. Then, both numerical solution and experimental measurement were processed to reconstruct the sound pressure at microphone position by applying the Rayleigh's integral. The three results (acoustic measurement with B&K microphone, Rayleigh's integral applied over measured and numerical data) are compared in Figure 40. A good superimposition of the curves can be observed, in particular above 300 Hz. At very low frequencies, below 200 Hz, one can note a turnaround of the microphone peaks with the laser evaluated ones. This is caused by the constructive and destructive reflections that affect the microphone measurement, which was not performed in anechoic room. The spectrum obtained by processing numerically calculated data does not present the peak at 550 Hz. This is most likely caused by the extreme ideality of the model: being the force on a nodal line, some modes are not excited, thus the peak does not appear.

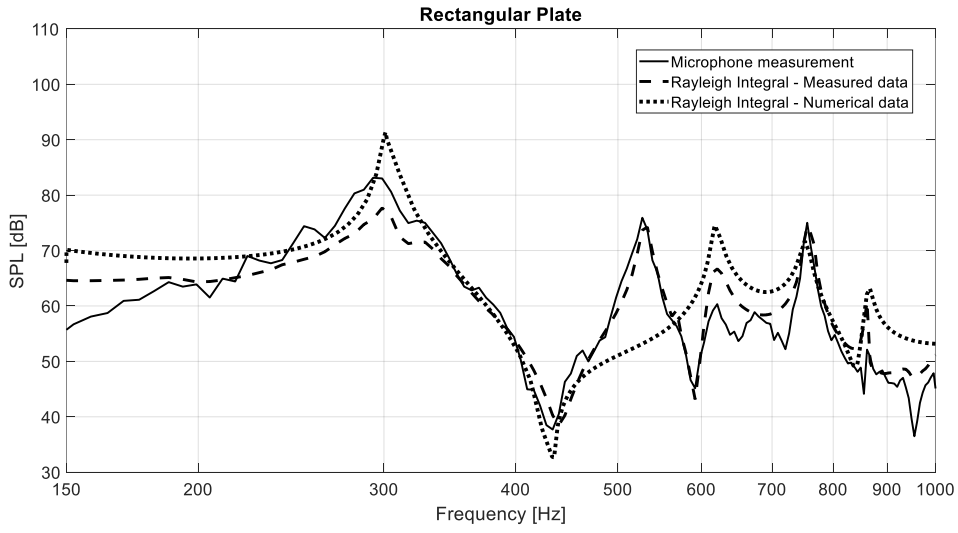

Figure 40. SPL recorded by microphone (solid line) superimposed with SPL calculated by Rayleigh integral for the measured data (coarse dash line) and the numerical Comsol data (narrow dash line).

4. Sound Generated by Real Vehicles' Panels: Analysis on a McLaren Supercar

Sound enhancement applications find increasing interest in the automotive field, thanks to the development of active noise control (ANC) [50] and active vibration control systems [24], [51]–[59], [60], [61]. Sound radiation produced by vibrating vehicle panels under electromagnetic shaker excitation deals with the second topic [62]–[69]. Aim of the research was the development of a fast, reliable method for the prediction of the sound field generated outside the vehicle by vibrating panels under electromagnetic shaker excitation. So, after the development of ideal conditions and simple structure models, the study continued with a real case problem. At McLaren research and development facilities, an analogue scheme was followed to test and validate the method on real vehicle's panels. On-vehicle measurements were acquired by exciting car panels both with impact hammer and mini-shakers and roving manually accelerometers on a test grid. A complete analysis was made on a P14R's aluminum hood, and the results are reported for this element.

4.1. Numerical FEM Model

The first step to produce the numerical Comsol model of the vehicle's hood was to simplify the original CATIA geometry, developed by McLaren. This task required many passages, which in the end resulted as outputs of a research on simulation software possibilities. The structure of the bonnet is made up of two separated layers, with slightly different thickness (1.1 mm for the inferior layer

and 0.9 mm for the upper one), bonded on the external border and in the middle reinforcement. In Figure 41 the two layers are depicted separately, to show the original configuration of their details.

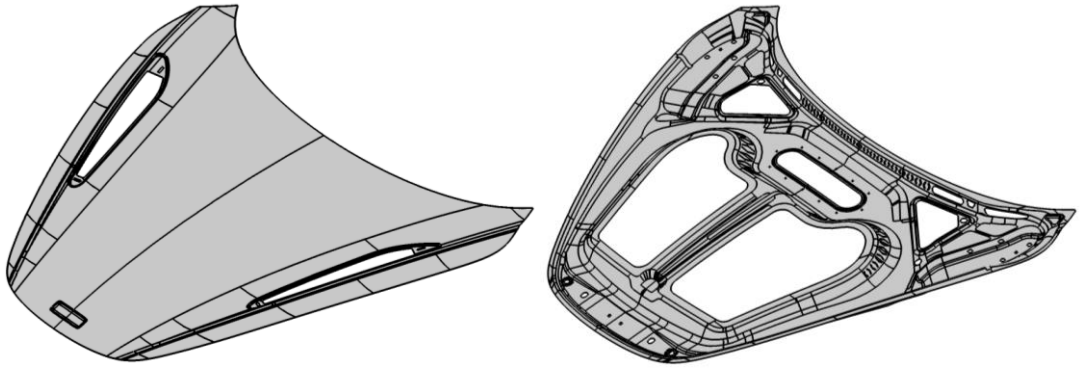

a) b)

Figure 41: Geometry of P14R bonnet, depicted with the two separated layers of which it's composed; a) upper layer and b) inferior layer.

The quantity of lines and micro details is needed for optimal design, but in terms of simulation is a flaw. The mesh would result very irregular and coarse regions could be alternated to extremely fine ones (Figure 42). Moreover, the possibility of occurring in mistakes due to intersecting lines is very high when drawings are so complex. At first, an attempt to simplify the structure was made in Hypermesh, since this software is equipped with a powerful mesh engine. A series of so-called "virtual operations" was carried out on the model to erase useless micro details and unite separated lines to form uniform patterns. The result, and most importantly the difference with Figure 42 is visible in Figure 43, where Hypermesh elaborated geometry is depicted after being meshed.

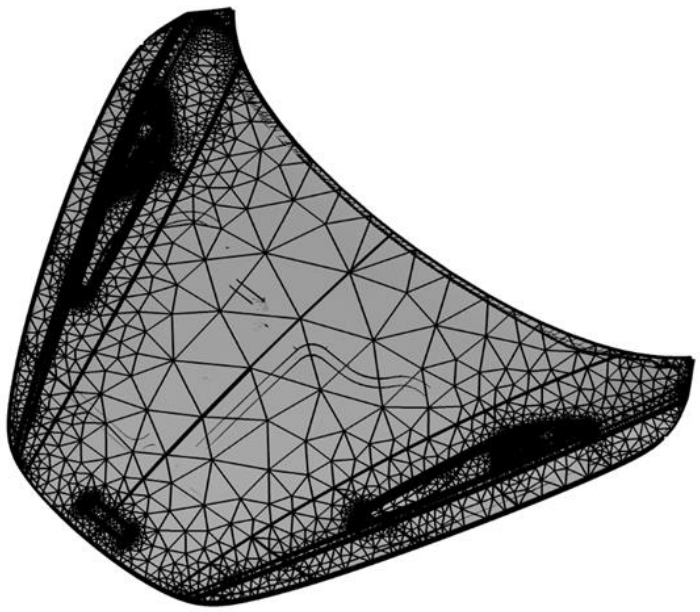

Figure 42: Meshing result in absence of "virtual operations". Coarse regions alternate with very narrow mesh ones.

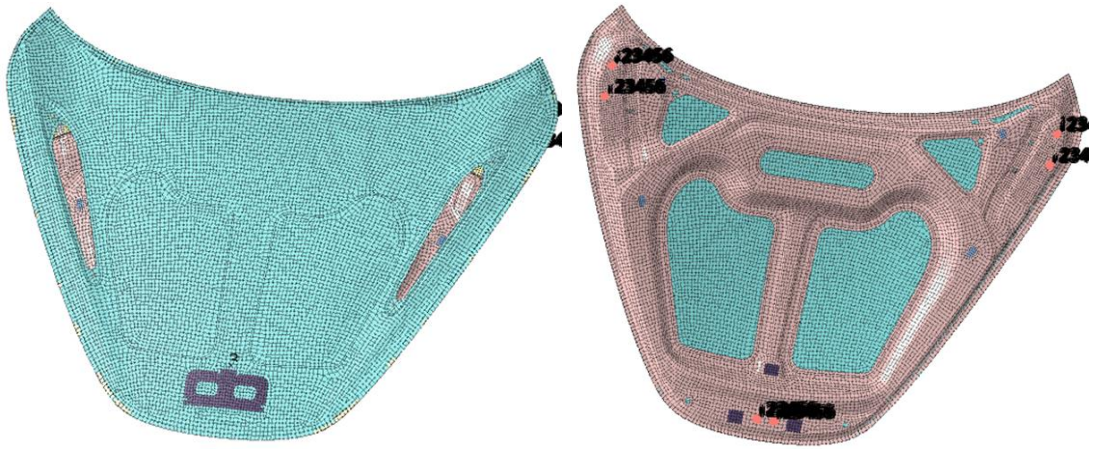

a) b)

Figure 43: Hypermesh meshed bonnet after the geometry has been improved and simplified. a) View from above; b) View from below.

Although the analysis with this software package would have been possible, it was opted to continue working in Comsol to have directly comparable results with the previously developed models. The first issue occurred during this step: the meshed model was exported in Nastran format to be imported and elaborated in Comsol, but once there, no changes could be applied. It was not possible to modify boundaries or to apply the harmonic force on the structure, thus it was opted to import the simplified model without mesh. It appeared soon

that the carried out “cleaning” operations done in Hypermesh were not exportable because of their intrinsic “virtual” nature. After several attempts, it was clearly inevitable the need of running the virtual operations directly in Comsol. The full geometry import process though, raised other problems as intersecting lines were constantly detected and the attempt to correct them all turned into an endless process. At this stage only one chance remained, namely, to import separately the upper and lower bonnet layers and to bond them in Comsol. An attempt to make the two layers work as an assembly in Hypermesh didn’t work either, since the bonding was not effective. This operation resulted more complicated than expected, as the reconstruction of the glue layer between the components didn’t have success. The “contact-adhesion” feature was adopted instead, as well as the “periodic condition” on the external borders. After a modal analysis run in Comsol, it was evident that those properties were not working correctly: the two layers were responding separately instead of moving together (Figure 44).

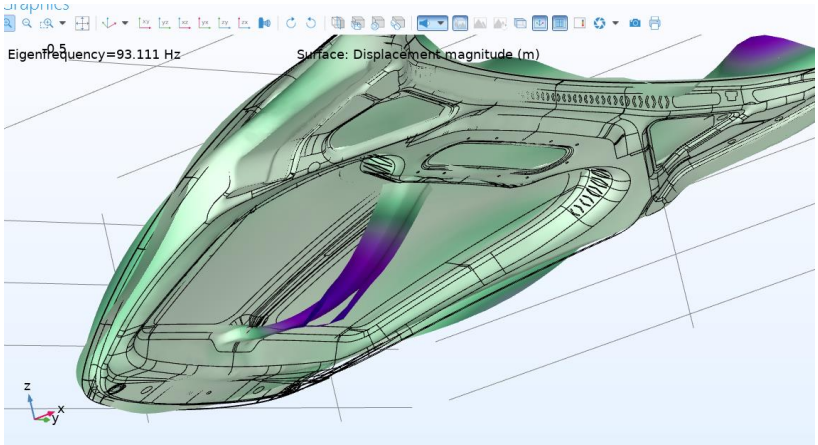

Figure 44: Modal analysis visualization for the displacement at 93.1 Hz, where it is clearly visible how the two layers don’t move united.

So, the final solution (Figure 45 a) was created as a simplification of the real structures bonding of the layers. The lower layer glue profile was extruded vertically to create a subtle foil that connects the two parts (Figure 45 b). This was the only way to make the layers work together, even if the elastic behaviour of the glue could not be correctly included in the model.

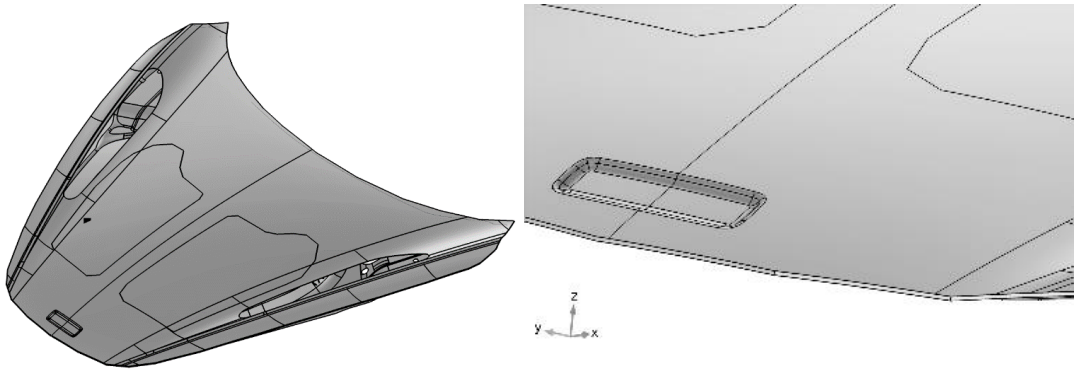

a) b)

Figure 45: The final developed model for the numerical simulation in Comsol. In a) the full geometry is depicted while in b) the extruded border detail is visible.

4.2. Impact Hammer Measurements

The first experimental analysis were carried out in a "traditional" way, namely impact hammer tests were carried out. A comparison with the subsequent shakers measurements was desired besides the usual modal analysis of the structure. An impact hammer type 8208 by Bruel&Kjaer was used, equipped with Teflon tip (the hardest available, which frequency response is shown in Figure 46). Four PCB 356A16 piezoelectric accelerometers, having a sensitivity of 100 mV/g were used to record the vibrational output (only vertical axis was recorded). This provided the normal acceleration data that were then employed to solve the Rayleigh's integral. As previously anticipated, it was decided to follow the same operational scheme of the simulations on rectangular plates. So, the bonnet was manually subdivided in a rectangular grid, at which nodes the accelerometers were placed to record the output to be post processed. A first set of measurements in mounted conditions was taken with an 8 cm resolution grid (Figure 47 a), namely a 160 nodes mesh, to verify the process in a reasonable time. According to the rule of Eq. 32, in this case it is possible to have correct solutions up to 714.58 Hz.

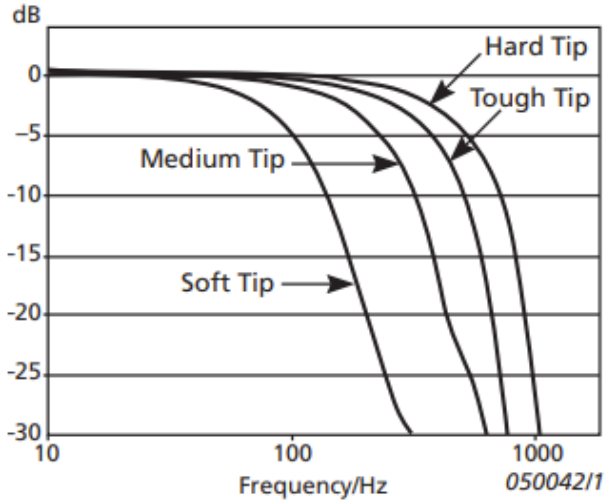

Figure 46: Frequency response functions of some tips for the Impact Hammer. Note: the Teflon tip is labeled as Hard Tip.

The acquisitions of the frequency response functions were run on TestLab Simulink (former LMS system) due to the possibility of analyzing real-time the signals' coherence and have direct visualization of the Frequency Response Functions (FRFs). To have high coherence data, a stiff point placed on a rib was chosen to excite the panel (yellow marker in Figure 47 a). The four accelerometers (Figure 47 b) were manually shifted on the grid starting from the left-top corner.

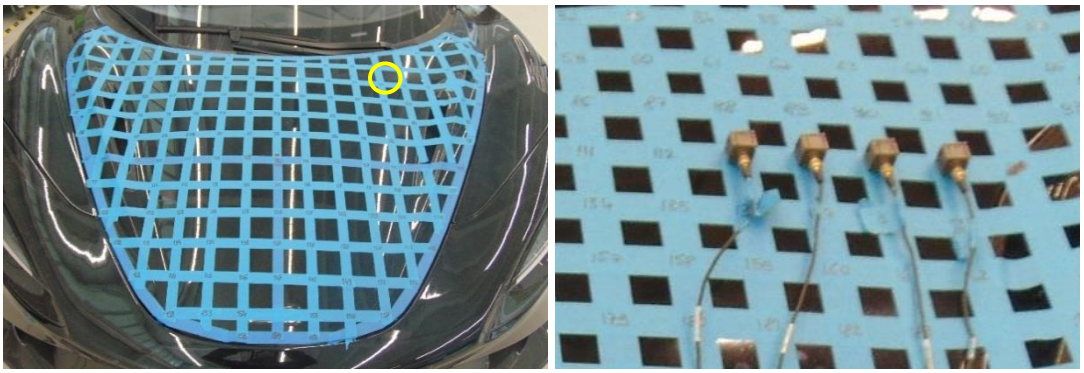

a) b)

Figure 47: The 8 cm grid that subdivided the hood in the mounted condition test and a) detail of the point application force (yellow circle) and b) the four adopted accelerometers.

Afterwards, the grid was refined to 5 cm resolution (that means with 368 nodes), to be able to reconstruct properly the emitted SPL up to 1 kHz. The tests in this case were two: bonnet in mounted conditions and free-free measurements.

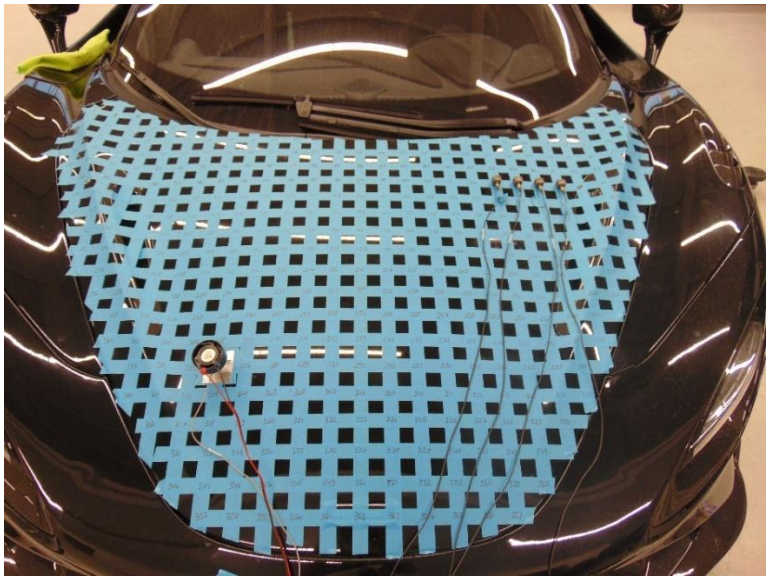

Figure 48: P14R bonnet subdivided by a 5 cm resolution grid, in mounted conditions.

After the first measurement set, the nodes with better FRFs and coherence were investigated to be able to choose other ones to excite in the subsequent tests. They were highlighted as depicted in Figure 49, where the free-free setup is visible.

During all the measurement sessions, a microphone (B&K type 4188, with 31.6 mV/Pa sensitivity) was placed above (for mounted condition) or in front (for free-free condition) of the bonnet's center at 1 meter distance. In the free-free measurement, the microphone acquisitions were recorded at 0.5 m distance too, to analyze the near field condition. The red circle in Figure 49 highlights the reference center point for the free-free measurement. Since the hammer was always impacting the same point (the accelerometers were roving), the microphone output was recorded during only half of the measurements, and then the extracted Noise Transfer Functions (NTFs) were averaged, to improve the signal to noise ratio.

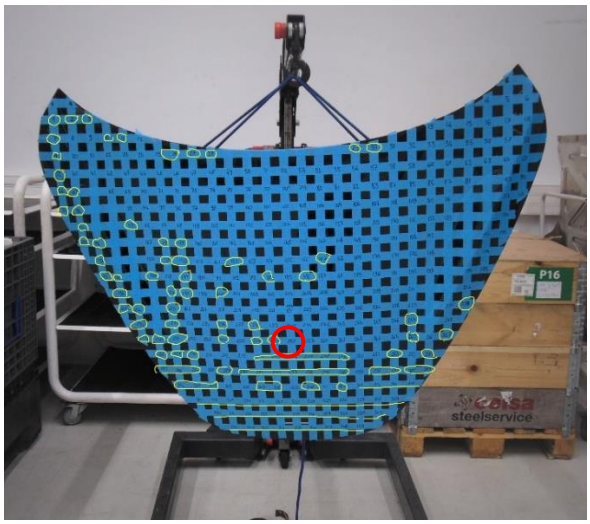

Figure 49: The bonnet hung in free free conditions with the possible force application points (yellow marks) and the reference center point for microphone position.

4.2.1. Results

Figure 50 shows the SPL outputs of the first set of measurements, with 8 cm grid in mounted bonnet conditions. Two curves are reported: the recorded microphone output in terms of NTF at 1 m distance, and the calculated SPL with Rayleigh's formula starting from the acceleration data recorded through the accelerometers in normal direction. The NTF is the average curve among all the recorded microphone acquisitions.

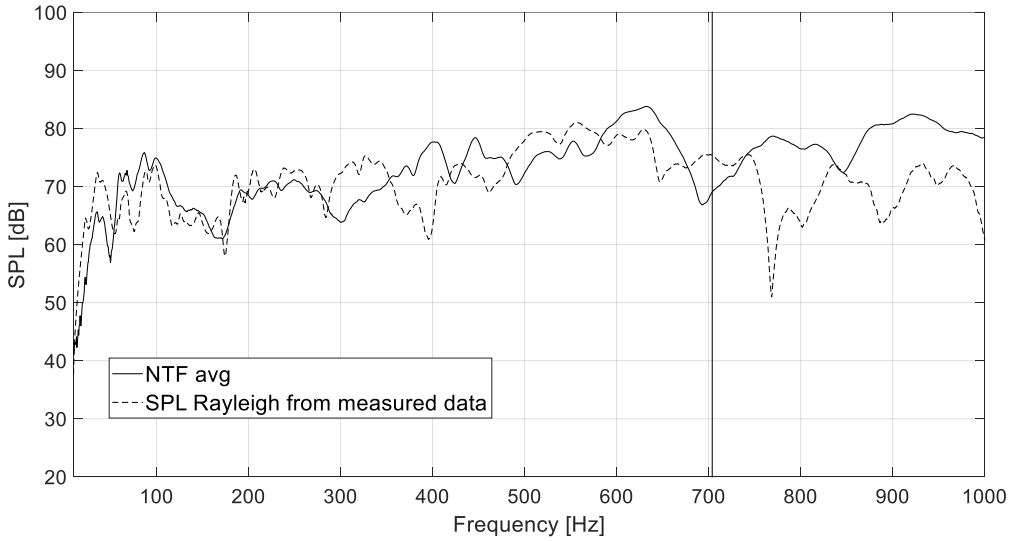

Figure 50: Superimposition of measurements results for the 8 cm grid impact test in mounted conditions at 1 m distance on axis: the solid line is the microphone output, seen as *noise transfer function* averaged over all the records, while the dashed line is the SPL curve calculated with Rayleigh's formula with acceleration input data from accelerometers records. The straight line at about 700 Hz indicates the validity of results limit for a grid of these dimensions.

It can be said that an excellent matching occurs at very low frequency, while some phase shifts occur between 350 and 450 Hz. Above 700 Hz a certain mismatch can be observed, but it is in accordance with the previously described mesh limits. In Figure 51 the data are depicted for the 5 cm grid solution. In this case less phase discordance can be observed but starting from about 600 Hz an important difference in dB occurs. A possible answer to this unexpected fact is that the hammer tip could not properly excite the panel at high frequencies.

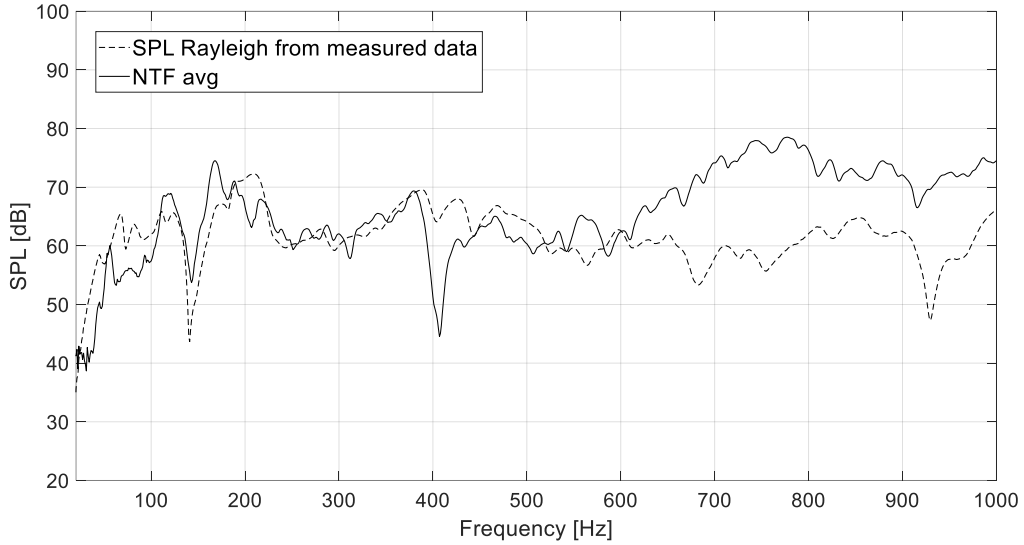

Figure 51: Superimposition of measurements results for the 5 cm grid impact test in mounted conditions at 1 m distance on axis: the solid line is the microphone output, seen as *noise transfer function* averaged over all the records, while the dashed line is the SPL curve calculated with Rayleigh's formula with acceleration input data from accelerometers records.

Figure 52 and Figure 53 show the free-free measurements results at two different distances: 0.5 m and 1 m on axis. Despite a similar trend of the curves', it can be stated that in both cases very good matching happens only at very low frequencies. It must be reminded that anyway, this test doesn't fully respect the boundary conditions required by Rayleigh's integral.

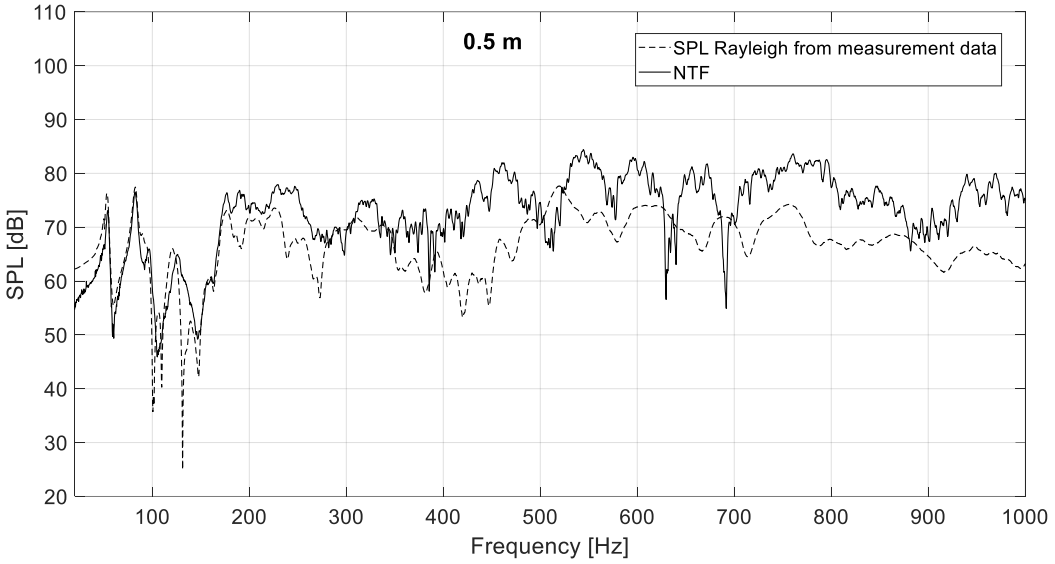

Figure 52: Superimposition of measurements results for the 5 cm grid impact test in free-free conditions at 0.5 m distance on axis: the solid line is the microphone output, seen as *noise transfer function* averaged over all the records, while the dashed line is the SPL curve calculated with Rayleigh's formula with acceleration input data from accelerometers records.

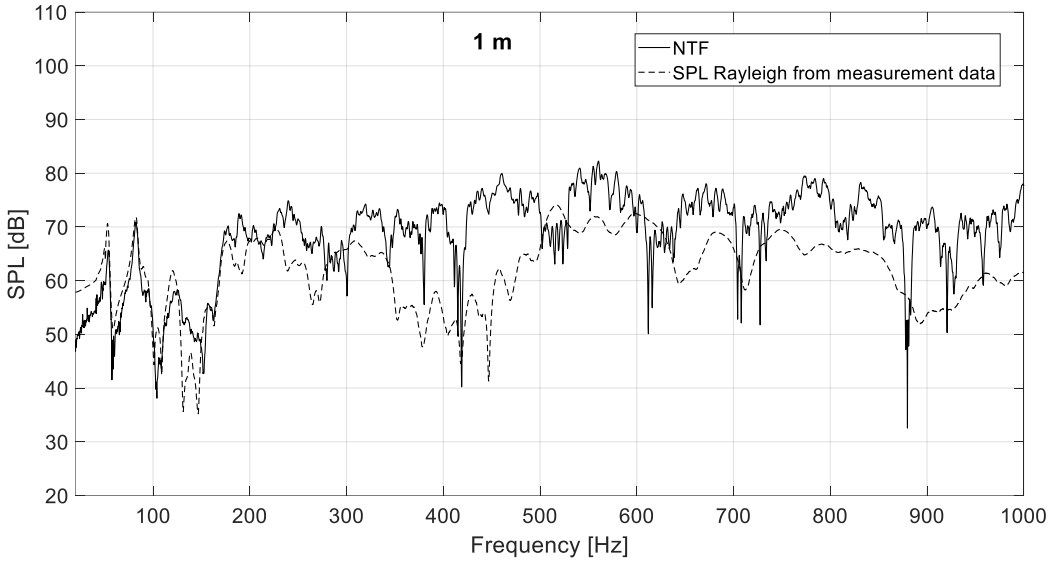

Figure 53: Superimposition of measurements results for the 5 cm grid impact test in free-free conditions at 1 m distance on axis: the solid line is the microphone output, seen as *noise transfer function* averaged over all the records, while the dashed line is the SPL curve calculated with Rayleigh's formula with acceleration input data from accelerometers records.

4.3. Measurements with Electro-Magnetic Shakers

The measurements were taken with a valuable mini shaker mounted on the aluminum bonnet and performed with accelerometers and microphones. This time the hood was tested just with the 5 cm resolution grid (Figure 54). The

shaker was positioned in the bottom-left corner of the panel, in a semi-rigid spot (Figure 55 a) while the accelerometers were manually shifted along all the nodes, starting from the upper-left corner. The system was driven by the Zoom F8 soundcard and mini amplifier previously described for the laboratory experiment, and the same ESS of 10 s was employed. The B&K microphone was positioned at the distance of 1 meter, on-axis with respect to the center of the bonnet (Figure 55 b), but a few records were acquired at 50 cm distance too.

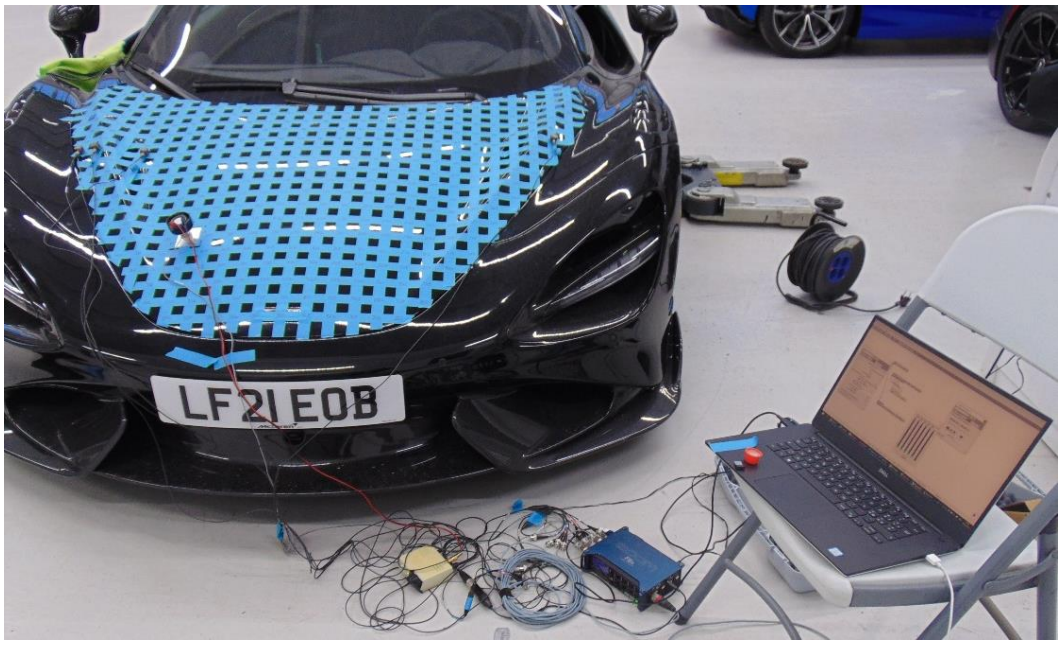

Figure 54: Measurement setup for the first set of tests with electromagnetic mini shaker. The Zoom F8 sound card is visible at the bottom of the picture, as well as the shaker's mini amplifier. On the car's hood the shaker is mounted as well as the four accelerometers.

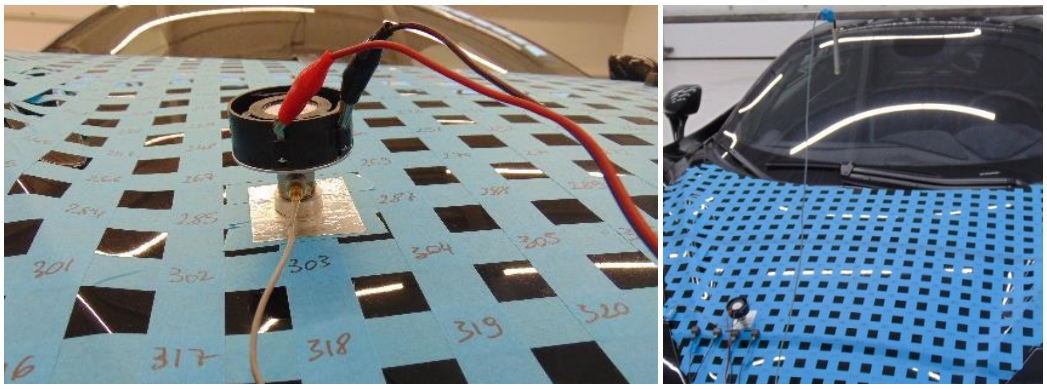

a) b)

Figure 55: Details of a) the mini shaker and b) microphone hung at 1 m distance from the centre of the bonnet.

4.3.1 Results

Below the results are presented for the described test. In Figure 56 one can observe the superimposition of the SPL curves obtained at 1 m distance on axis. The recorded (and averaged) noise transfer function is quite well matched with the sound pressure level calculated from the acceleration data with Rayleigh's approximation, despite some phase discrepancies and dB mismatches. The most important thing to be observed, is the good correlation also in the frequency range 600 Hz – 1 kHz, which was not happening with the impact hammer tests outputs. Figure 57 shows a comparison between the two analyzed distances (0.5 m and 1 m). The straight vertical lines indicate the theoretical limit for far field condition. As expected, the output related to 1 m distance correlates better with the acoustic measurement, since the far field is an implied condition of Rayleigh's integral solution.

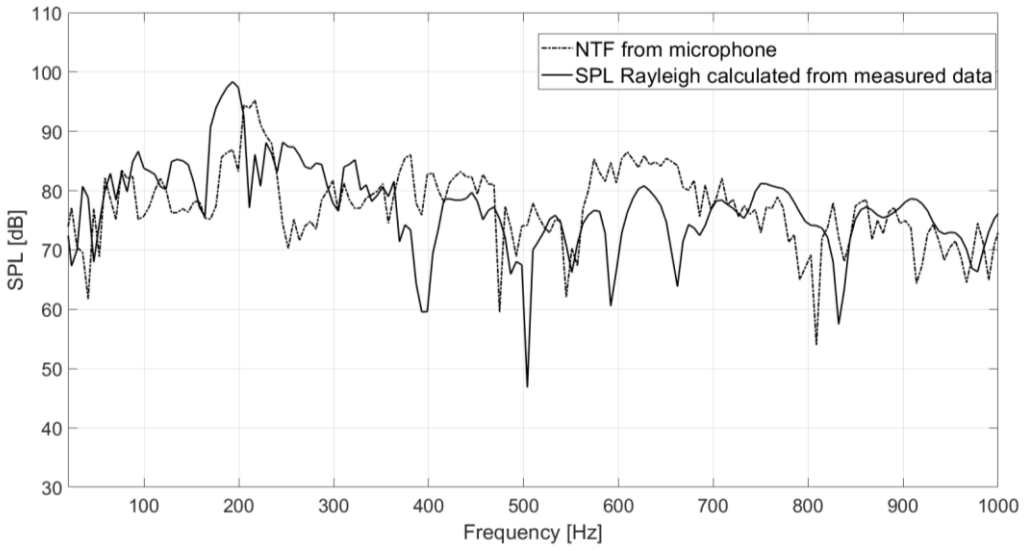

Figure 56: Superimposition of measurements results for the 5 cm grid electromagnetic shaker test in mounted conditions at 1 m distance on axis: the dashed line is the microphone output, seen as *noise transfer function* averaged over all the records, while the solid line is the SPL curve calculated with Rayleigh's formula using acceleration data from accelerometers records.

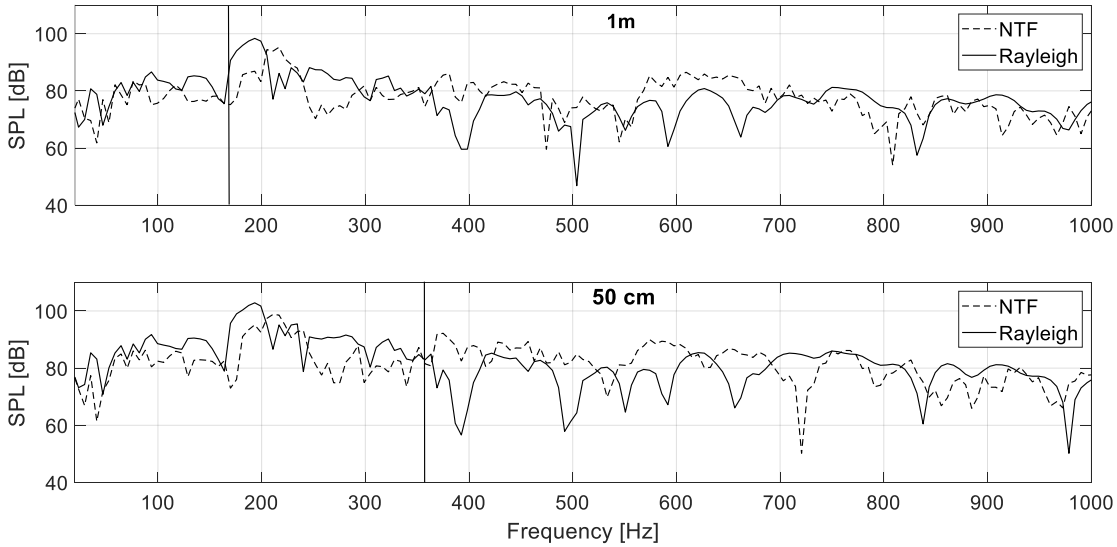

Figure 57: Comparison of the results at two different microphonic distances: at 1 m distance (above) and 0.5 m (below). The noise transfer functions are superimposed to the calculated SPL starting from experimental acceleration data. Theoretical limits for far field condition are highlighted with straight vertical lines.

4.4 Comparison Between Experimental and Mixed Method Results

A second set of measurements was realized with the mini shaker, addressed to the validation of the mixed method for SPL evaluation. The tests were carried out without accelerometers recording, exciting the hood in five different positions (Figure 58), and the acceleration data were directly calculated in the numerical Comsol model. They were then extracted on a grid of points defined in Matlab in order to make them coincide with the mesh nodes, to have the most precise possible result. This "evaluation grid" (Figure 59) was then extracted and used as acceleration (or better, *accelerance*, since the analysis was run in frequency domain) input matrix for Rayleigh's formula.

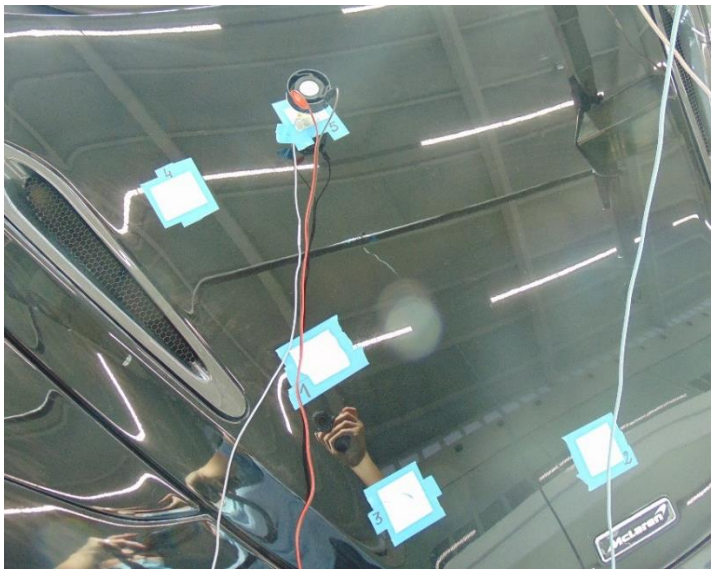

Figure 58: The five excitation points for the mixed method testing.

In Figure 60 the superimposition of the calculated sound pressure level curves is shown for the first tested point (number 1 of Figure 58): under 250 Hz and above 800 Hz the matching is not verified, meanwhile in the spectrum's central region the curves' trend matches quite well. Points number 2 and 3 (Figure 61 and Figure 62) had a better signal's coherence (they lay in a stiffer region compared to all the others). This is the most important reason for the improved correlation between the recorded SPL and the calculated one. It must also not be forgotten that the numerical model presents some simplifications (mainly the absence of a glue layer substituted by an aluminium vertical extrusion) that don't correspond to reality.

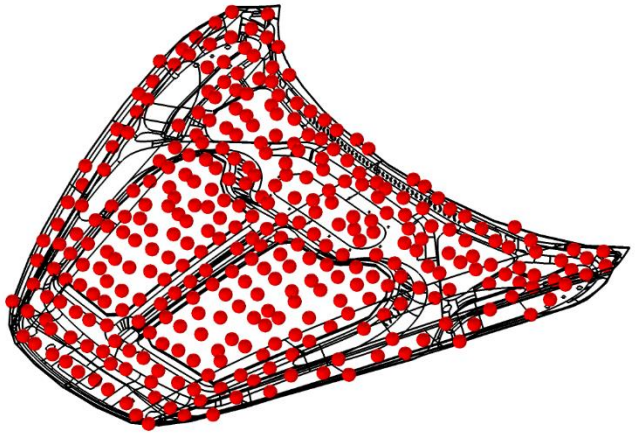

Figure 59: The Comsol model intersected by the "evaluation grid" of points where the acceleration data are extracted.

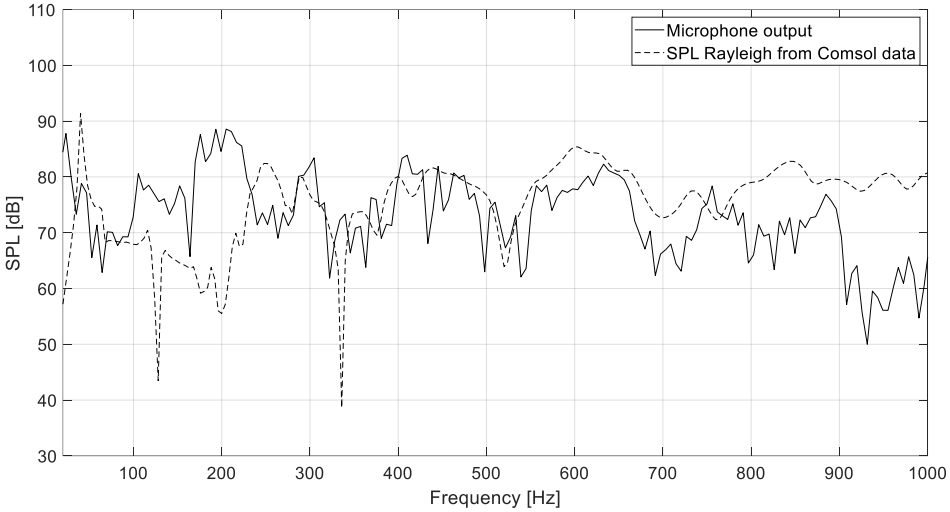

Figure 60: Superimposition of recorded SPL at 1m distance and calculated curve with numerical and analytical mixed process, for shaker placed in point 1.

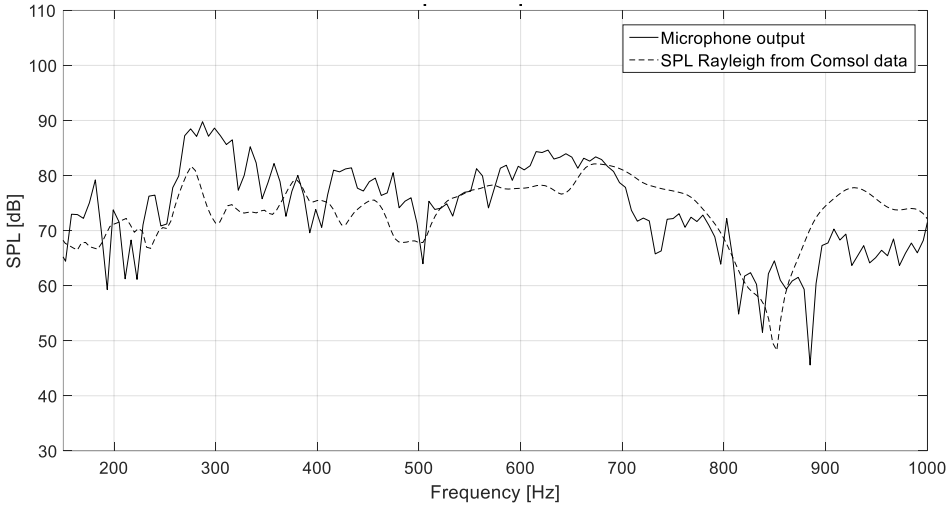

Figure 61: Superimposition of recorded SPL at 1m distance and calculated curve with numerical and analytical mixed process, for shaker placed in point 2.

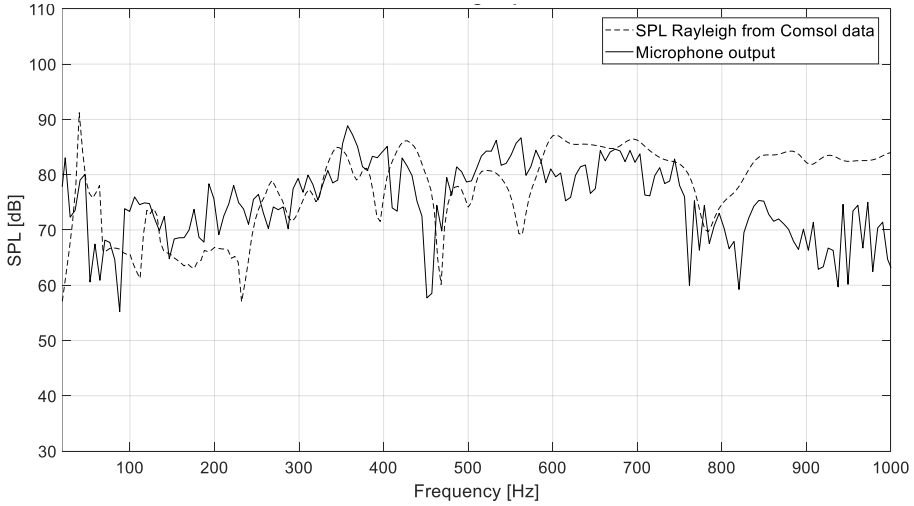

Figure 62: Superimposition of recorded SPL at 1m distance and calculated curve with numerical and analytical mixed process, for shaker placed in point 3.

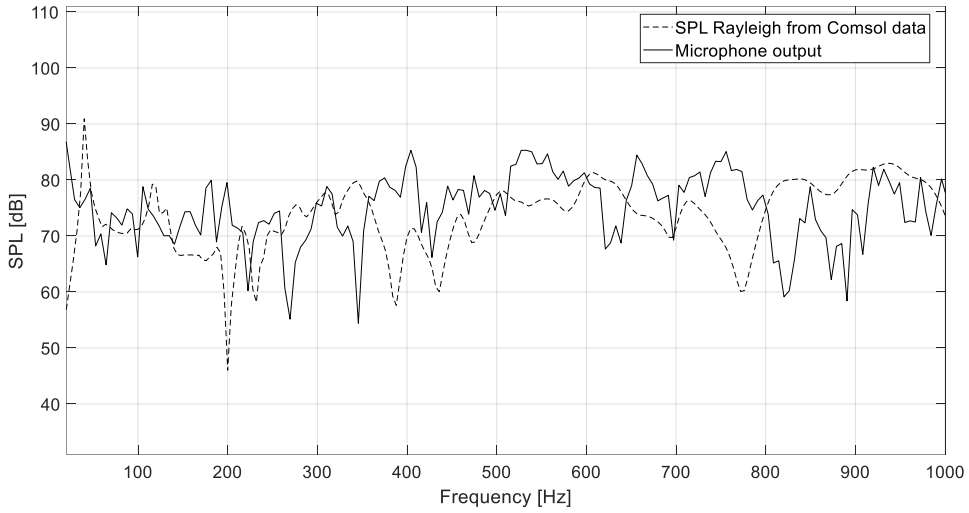

Figure 63: Superimposition of recorded SPL at 1m distance and calculated curve with numerical and analytical mixed process, for shaker placed in point 4.

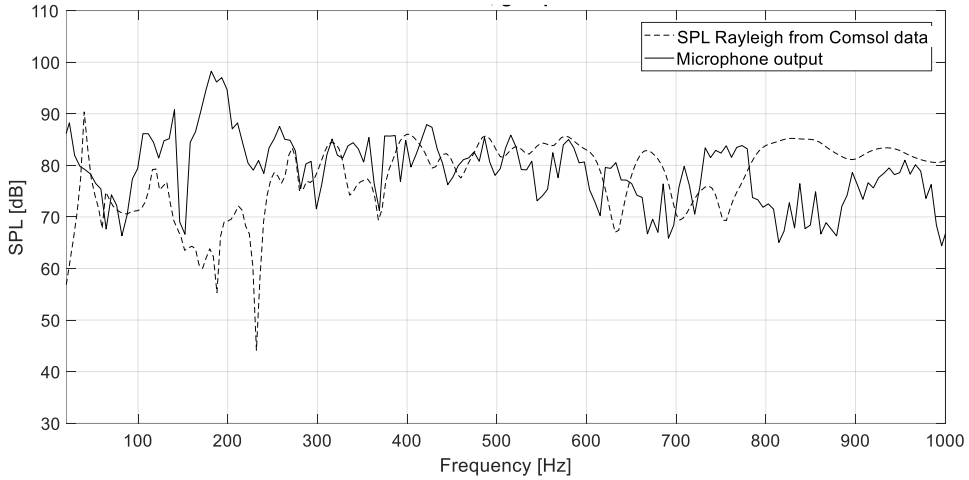

Figure 64: Superimposition of recorded SPL at 1m distance and calculated curve with numerical and analytical mixed process, for shaker placed in point 5.

5. Sound Spatiality Analysis for Active Sound Enhancement

5.1. Directivity Analysis of the Vehicle Excited at the Bonnet

The next step to aim at the development of an efficient sound enhancement system was to study the spatial behaviour of the radiated sound pressure from the bonnet excited by the mini shaker. The directivity was studied applying the force in the same two positions of the measurements shown in Section 3. It was not possible to perform the measurements in a semi-anechoic room (reflecting floor and absorbing walls and ceiling), which is the facility usually employed for acoustic measurement in automotive industry. However, the car was placed outdoor in free field in an asphalted square, which provides a very similar condition. The equipment was substantially the same of the previous measurements, i.e. the test chain was composed of:

- a high-performance laptop
- a Zoom F8 audio card
- a mini shaker with mini power amplifier
- a B&K microphone type 4188 with preamplifier type 2671

Since the information is only relevant in the front part of the vehicle (in this case), the measurement was performed on a front semi circumference, having a radius of 1.5 m from the centre of the bonnet, instead of all around the vehicle. The microphone was placed on a 1.2 m high tripod, shifted by 10 degrees steps (Figure 65). The mini amplifier was set at 2 Volt in both cases. Since the Exponential Sine Sweep once again demonstrated to be a valid and solid test method, the input signal was a 10 second ESS from 20 Hz to 10 kHz, due to the interested frequency range of application. The polar patterns in octave bands

elaborated from the two measurements' results are shown in Figure 66 and Figure 67, respectively for the shaker placed at bottom left and bottom centre of the hood. As one can see, applying the force at bottom left, the directivity appears to be strongly asymmetrical (Figure 66). A lobe is clearly pointing towards the angle at 330° in the 2 kHz, 4 kHz, and 8 kHz octave bands. This is the angle between the direction passing through the point of application and the centre of the hood and the axis of symmetry of the hood itself. Instead, two lobes are prominent at low frequencies, in the 63 Hz and 250 Hz bands, mainly at angles 330° and 60°. In these two octave bands, the highest radiation efficiency is observed, too.

Figure 65: Measurement setup for directivity tests.

Moving the force application point at bottom centre position, the radiation pattern becomes more omnidirectional (Figure 67). The biggest discrepancy can be noticed in the 250 Hz band, where the efficiency drops significantly, and in the 500 Hz band, where instead it increases considerably. On the contrary, 63 Hz, 1 kHz and 4 kHz bands maintain a similar radiation efficiency to the previous case.

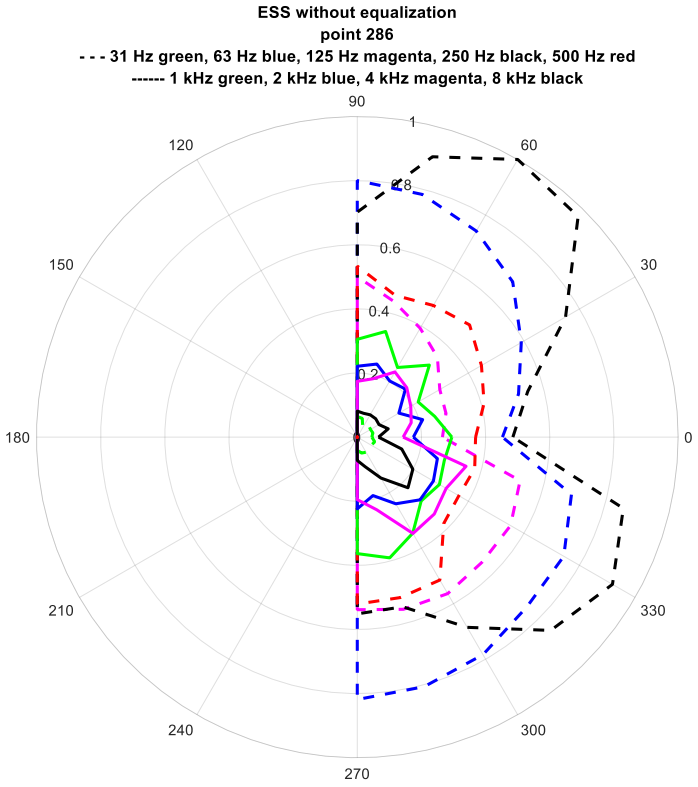

Figure 66: Polar directivity pattern in octave bands for the bottom-left point excited with non-equalized ESS.

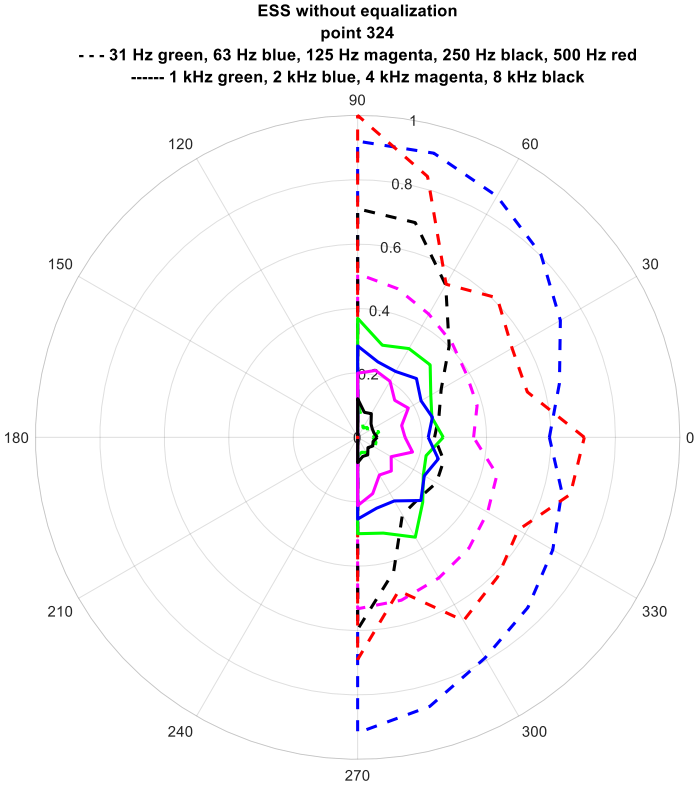

Figure 67: Polar directivity pattern in octave bands for the bottom-center point excited with non-equalized ESS.

5.2. Pre-Equalization of ESS

It was opted to evaluate the influence of a pre-equalization of the system. In fact, both the transducer's properties and the response of the panel affect the measurement's results, mainly in terms of non-flat frequency response. The best way to avoid this effect is to equalize the sound source's frequency response, i.e. to flatten its spectrum. There are several techniques to do so, but in this work the Kirkeby inversion method was applied (see Section 2.6).

The ESS was played in both shaker's positions and recorded by the microphone in front of the bonnet (0 degrees on the charts in Figure 66 and Figure 67). The output was then processed via Matlab to perform the inversion algorithm. In particular:

1. The signal was convolved with the inverse ESS (a time reverse, pre-equalized version of the original ESS) and the obtained impulse response was cut with reasonable length to keep as much information as possible at low frequency (Figure 68), together with avoiding at best the reverberation, which would cause artefacts when applying Kirkeby's algorithm.
2. The windowed IR was then transformed into frequency domain and inverted according to Kirkeby's algorithm, obtaining the equalizing impulse response (Figure 69).
3. Convolving the ESS with the new FIR filter, the desired flat spectrum was calculated in the chosen frequency range (from 200 to 900 Hz in this case), as depicted in Figure 70.
4. The pre-equalized ESS was played by the shaker and recorded.

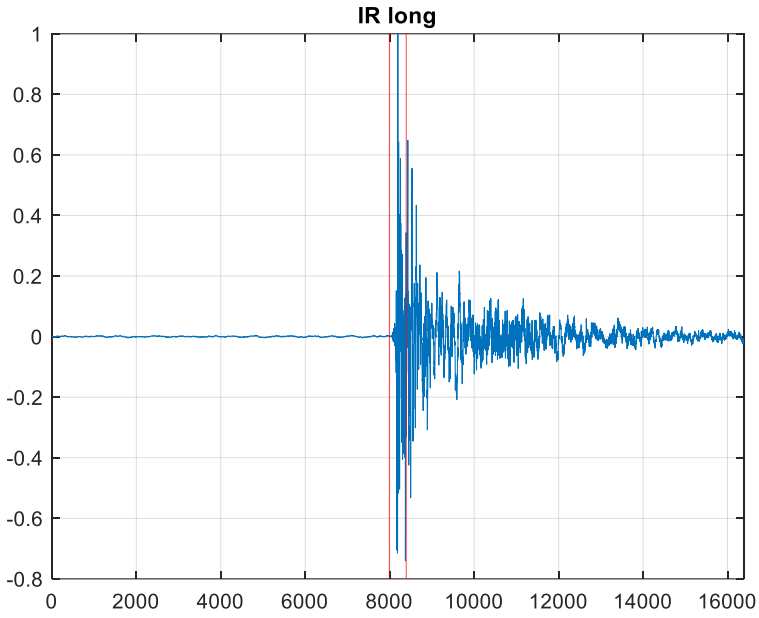

a)

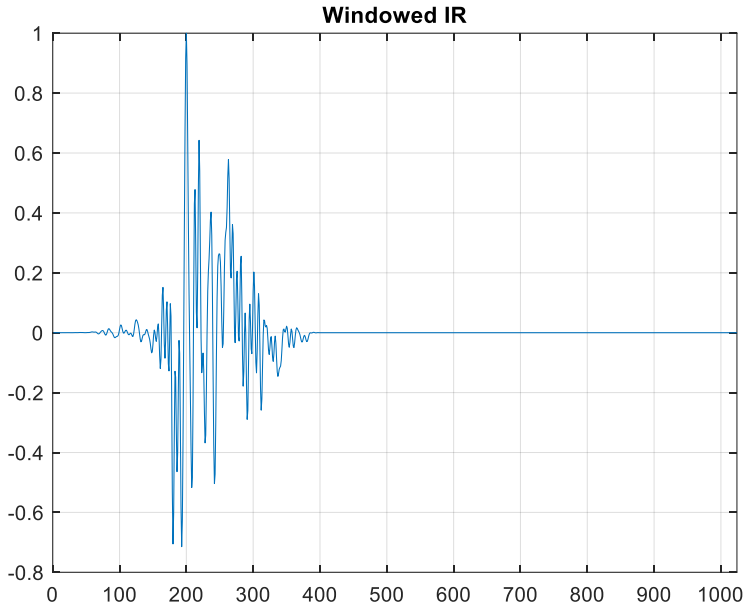

b)

Figure 68: a) Example of full-length impulse response in time domain and b) windowed IR.

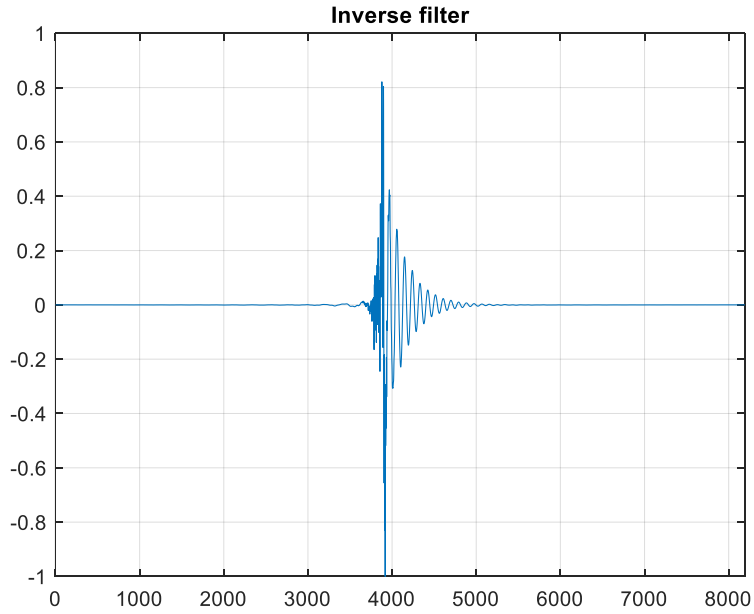

a)

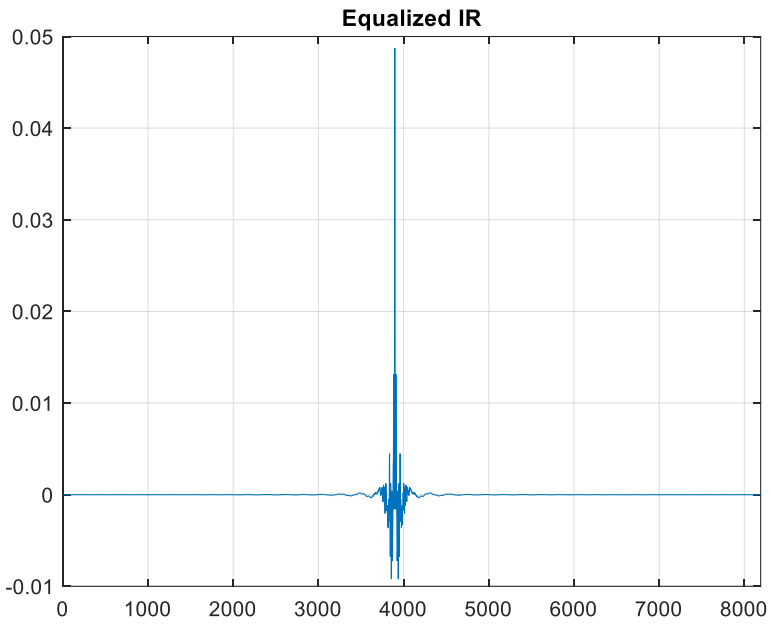

b)

Figure 69: a) Example of inverse filter to apply to get b) equalized IR.

The result of this procedure is shown in fig Figure 71 and Figure 72, respectively for the shaker placed at bottom left and bottom centre of the bonnet. In Figure 70 one can note that the spectrum of the equalization filter (red curve) is opposite to the one the windowed IR (blue curve), in the frequency range of inversion, which is 200 Hz – 900 Hz. In the same range, it is visible that the equalization produced a flat spectrum (yellow curve).

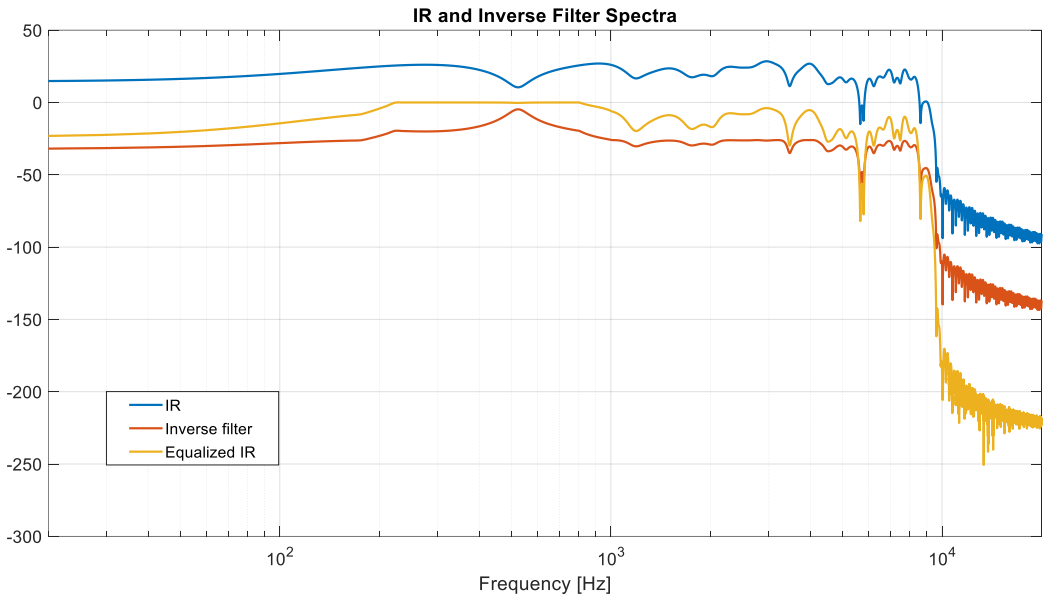

Figure 70: Visualization of impulse response (blue), the inverse Kirkeby filter to be applied (red) and the resulting equalized impulse response (yellow). The equalization is comprised between 200 and 800 Hz.

In principle, the pre distortion of the spectrum should make the polar plot match in one point for the equalized frequency bands, in correspondence of the angle where the calibrated signal was recorded (in this case, 0 angle, hence in front of the bonnet). This result would be obtained by selecting from the IR only the direct sound, discarding all the reflections, which is usually feasible when dealing with loudspeakers in anechoic room measurements. In this case, instead, the long reverberation of the panel and the proximity of the reflecting floor makes almost impossible to achieve such separation. This effect is particularly evident for low frequencies, where the damping of the panel is lower and the acoustic wavelength in air is longer. As a result, one can note that radiation patterns match almost only at high frequency: from 500 Hz to 8 kHz octave bands for the out-axis case (Figure 71) and from 1 kHz to 4 kHz octave bands for the in-axis case (Figure 72). However, a very good matching can be observed for the 63 Hz and 250 Hz octave bands in the out-axis case and for the 63 Hz and 500 Hz octave bands in the in-axis case.

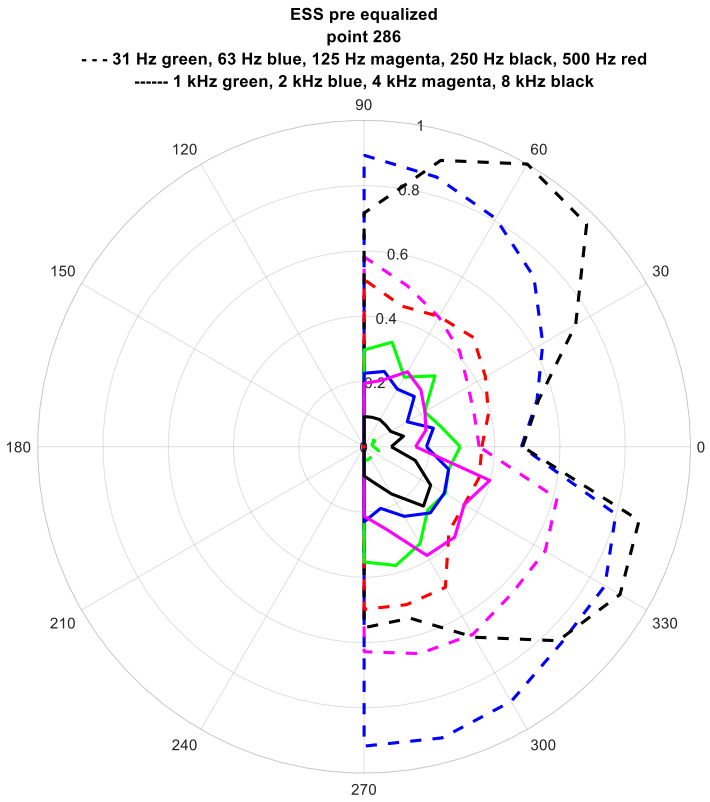

Figure 71: Polar directivity pattern in octave bands for the bottom-left point excited with pre-equalized ESS.

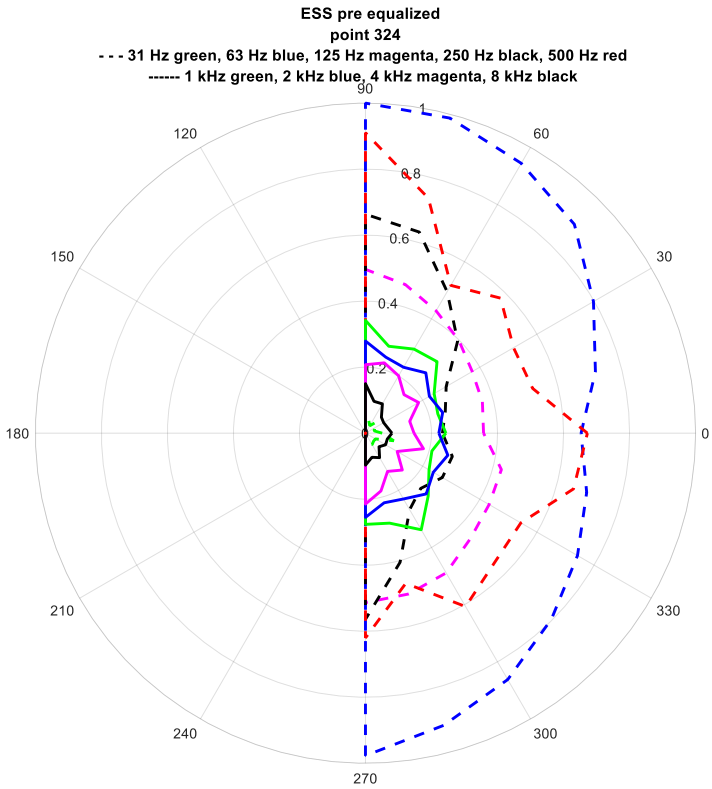

Figure 72: Polar directivity pattern in octave bands for the bottom-center point excited with pre-equalized ESS.

6.Conclusion and Future Developments

A fast and reliable method for predicting the exterior sound field generated by vehicle panels excited with electrodynamic shakers in steady state was developed and validated. It makes use of a mechanical simulation of a single vibrating panel and the solution of Rayleigh's integral where the numerical solution was previously evaluated.

At first, the technique was demonstrated through laboratory measurements using a flat aluminium plate, fully clamped in a wooden baffle. A mechanical measurement with a LDV, an acoustic measurement with a microphone, and a numerical FEM simulation were compared. Then, a real vehicle panel was tested, replacing the LDV with manually moved piezo-electric accelerometers. In both laboratory and on-vehicle tests, a very good agreement was found between experimental measurements and numerical or analytical-numerical solutions.

The mixed method allows for calculating the numerical solution of the vibration of a single panel, without including the car geometry for front and rear radiation separation, neither a surrounding air volume, which would be necessary as solution domain. In this way, it is possible to exclude the undesired effect of the acoustic short-circuit and, at the same time, to reduce considerably the complexity of the model together with computational time.

This method can be exploited as fast and reliable tool for the analysis of sound enhancement systems, like acoustic vehicle alert systems (AVAS), which are necessary for the new generation of "silent" vehicles.

7.Bibliography

[1] F. Fahy and P. Gardonio, "1 - Waves in Fluids and Solid Structures," in *Sound and Structural Vibration (Second Edition)*, Second Edition., F. Fahy and P. Gardonio, Eds. Oxford: Academic Press, 2007, pp. 1–73. doi: https://doi.org/10.1016/B978-012373633-8/50005-3.

[2] W. Klippel and J. Schlechter, "Measurement and Visualization of Loudspeaker Cone Vibration," *Audio Engineering Society - 121st Convention Papers 2006*, vol. 1, Jan. 2006.

[3] F. Fahy and P. Gardonio, "2 - Structural Mobility, Impedance, Vibrational Energy and Power," in *Sound and Structural Vibration (Second Edition)*, F. Fahy and P. Gardonio, Eds. Oxford: Academic Press, 2007, pp. 75–134. doi: https://doi.org/10.1016/B978-012373633-8/50006-5.

[4] P. Sun, H. Yang, and Y. Zhao, "Time-domain calculation method of improved hysteretic damped system based on frequency-dependent loss factor," *J Sound Vib*, vol. 488, p. 115658, 2020, doi: https://doi.org/10.1016/j.jsv.2020.115658.

[5] A. W. Leissa, "The historical bases of the Rayleigh and Ritz methods," *J Sound Vib*, vol. 287, no. 4, pp. 961–978, 2005, doi: https://doi.org/10.1016/j.jsv.2004.12.021.

[6] A. W. Leissa, "The free vibration of rectangular plates," *J Sound Vib*, vol. 31, no. 3, pp. 257–293, 1973, doi: https://doi.org/10.1016/S0022-460X(73)80371-2.

[7] C.-C. Sung and J. T. Jan, "THE RESPONSE OF AND SOUND POWER RADIATED BY A CLAMPED RECTANGULAR PLATE," *J Sound Vib*, vol. 207, no. 3, pp. 301–317, 1997, doi: https://doi.org/10.1006/jsvi.1997.1125.

[8] N. Li, “Forced vibration analysis of the clamped orthotropic rectangular plate by the superposition method,” *J Sound Vib*, vol. 158, no. 2, pp. 307–316, 1992, doi: https://doi.org/10.1016/0022-460X(92)90053-Z.

[9] A. Rahbar Ranji and H. Rostami Hoseynabadi, “A semi-analytical solution for forced vibrations response of rectangular orthotropic plates with various boundary conditions,” *Journal of Mechanical Science and Technology*, vol. 24, no. 1, pp. 357–364, 2010, doi: 10.1007/s12206-009-1010-3.

[10] I. Senjanović, M. Tomic, N. Vladimir, and N. Hadžić, “An Analytical Solution to Free Rectangular Plate Natural Vibrations by Beam Modes – Ordinary and Missing Plate Modes,” *Transactions of FAMENA*, vol. 40, pp. 1–18, Nov. 2016, doi: 10.21278/TOF.40301.

[11] M. C. Heilemann, D. Anderson, and M. F. Bocko, “Sound-source localization on flat-panel loudspeakers,” *AES: Journal of the Audio Engineering Society*, vol. 65, no. 3, pp. 168–177, Oct. 2017, doi: 10.17743/jaes.2016.0066.

[12] Z. Li, P. Luo, C. Zheng, and X. Li, “Vibrational Contrast Control for Local Sound Source Rendering on Flat Panel Loudspeakers,” *Journal of The Audio Engineering Society*, 2018.

[13] D. Anderson and M. Bocko, *A Model for the Impulse Response of Distributed-Mode Loudspeakers and Multi-Actuator Panels*. 2015.

[14] C. Hatiegan, G.-R. Gillich, E. Raduca, M. Nedeloni, and L. Cîndea, “Equation of Motion and Determining the Vibration Mode Shapes of a Rectangular Thin Plate Simply Supported on Contour Using MATLAB,” *Annals of the University ,, Eftimie Murgu” Resita,* vol. XX, Jan. 2013.

[15] D. J. Gorman, “Accurate analytical type solutions for the free in-plane vibration of clamped and simply supported rectangular plates,” *J Sound Vib*, vol. 276, no. 1, pp. 311–333, 2004, doi: https://doi.org/10.1016/j.jsv.2003.07.037.

[16] S. Cecchi, A. Terenzi, F. Piazza, and F. Bettarelli, *Applying Sound Equalization to Vibrating Sound Transducers Mounted on Rigid Panels*. 2019.

[17] S. Cecchi, A. Terenzi, F. Piazza, and F. Bettarelli, "Applying Sound Equalization to Vibrating Sound Transducers Mounted on Rigid Panels." [Online]. Available: http://www.aes.org/e-lib

[18] M. Eisenberger and A. Deutsch, "Solution of thin rectangular plate vibrations for all combinations of boundary conditions," *J Sound Vib*, vol. 452, pp. 1–12, Oct. 2019, doi: 10.1016/j.jsv.2019.03.024.

[19] M. P. Norton and J. Pan, "NOISE | Noise Radiated by Baffled Plates," *Encyclopedia of Vibration*. Elsevier, pp. 887–898, 2001. doi: 10.1006/rwvb.2001.0146.

[20] A. Brandt, *Noise and Vibration Analysis: Signal Analysis and Experimental Procedures*. Wiley, 2011. [Online]. Available: https://books.google.it/books?id=-1DSxrlhL5sC

[21] J. Arenas, "On the vibration analysis of rectangular clamped plates using the virtual work principle," *Journal of Sound and Vibration - J SOUND VIB*, vol. 266, pp. 912–918, Sep. 2003, doi: 10.1016/S0022-460X(03)00056-7.

[22] S. M. Kirkup, "Computational solution of the acoustic field surrounding a baffled panel by the Rayleigh integral method," *Appl Math Model*, vol. 18, no. 7, pp. 403–407, 1994, doi: https://doi.org/10.1016/0307-904X(94)90227-5.

[23] W. Klippel and J. Schlechter, "Distributed Mechanical Parameters Describing Vibration and Sound Radiation of Loudspeaker Drive Units."

[24] C.-C. Sung and C. T. Jan, "Active control of structurally radiated sound from plates," *J Acoust Soc Am*, vol. 102, no. 1, pp. 370–381, Jul. 1997, doi: 10.1121/1.419759.

[25] F. Fahy and P. Gardonio, "3 - Sound Radiation by Vibrating Structures," in *Sound and Structural Vibration (Second Edition)*, F. Fahy and P. Gardonio, Eds. Oxford: Academic Press, 2007, pp. 135–241. doi: https://doi.org/10.1016/B978-012373633-8/50007-7.

[26] P. M. Juhl, “Radiation of sound.” 2011. [Online]. Available: https://www.researchgate.net/publication/229025696

[27] W. Klippel and J. Schlechter, “Distributed Mechanical Parameters of Loudspeakers Part 1: Measurements,” *AES: Journal of the Audio Engineering Society*, vol. 57, pp. 500–511, Jul. 2009.

[28] L. Čurović, J. Murovec, T. Novaković, R. Prislan, and J. Prezelj, “Time–frequency methods for characterization of room impulse responses and decay time measurement,” *Measurement*, vol. 196, p. 111223, 2022, doi: https://doi.org/10.1016/j.measurement.2022.111223.

[29] A. Farina, “Simultaneous Measurement of Impulse Response and Distortion with a Swept-Sine Technique,” in *108th Convention*, 2000, pp. 1–24.

[30] J. W. Draper III and S. W. Lee, “Smooth construction of impulse response functions and applied loads using a time domain deconvolution method,” *J Sound Vib*, vol. 443, pp. 430–443, 2019, doi: https://doi.org/10.1016/j.jsv.2018.11.050.

[31] Y. Champoux, V. Cotoni, B. Paillard, and O. Beslin, “Moment excitation of structures using two synchronized impact hammers,” *J Sound Vib*, vol. 263, no. 3, pp. 515–533, 2003, doi: https://doi.org/10.1016/S0022-460X(02)01064-7.

[32] S. J. Ahn, W. B. Jeong, and W. S. Yoo, “Unbiased expression of FRF with exponential window function in impact hammer testing,” *J Sound Vib*, vol. 277, no. 4, pp. 931–941, 2004, doi: https://doi.org/10.1016/j.jsv.2003.09.022.

[33] X. Wei, J. Zhang, S. Živanović, J. Liu, J. Russell, and X. He, “Dynamic properties of impact hammer operator and their influence on dynamics of lightweight structures,” *J Sound Vib*, vol. 529, p. 116932, 2022, doi: https://doi.org/10.1016/j.jsv.2022.116932.

[34] G. Liu, J. Cong, P. Wang, S. Du, L. Wang, and R. Chen, "Study on vertical vibration and transmission characteristics of railway ballast using impact hammer test," *Constr Build Mater*, vol. 316, p. 125898, 2022, doi: https://doi.org/10.1016/j.conbuildmat.2021.125898.

[35] M. C. Bellini, L. Collini, A. Farina, D. Pinardi, and K. Riabova, "Measurements of loudspeakers with a laser doppler vibrometer and the exponential sine sweep excitation technique," *AES: Journal of the Audio Engineering Society*, vol. 65, no. 7–8, 2017, doi: 10.17743/jaes.2017.0017.

[36] A. Farina, S. Campanini, L. Chiesi, A. Amendola, and L. Ebri, "Spatial sound recording with dense microphone arrays," in *AES 55th International Conference*, 2014, pp. 1–8.

[37] J. Maierhofer, A. el Mahmoudi, and D. Rixen, *DEVELOPMENT OF A LOW COST AUTOMATIC MODAL HAMMER FOR APPLICATIONS IN SUBSTRUCTURING*. 2019. doi: 10.13140/RG.2.2.21408.43527.

[38] Q. Meng, D. Sen, S. Wang, and L. Hayes, *Impulse response measurement with sine sweeps and amplitude modulation schemes*. 2009. doi: 10.1109/ICSPCS.2008.4813749.

[39] A. Farina, "Silence Sweep: a novel method for measuring electro-acoustical devices," Oct. 2022.

[40] M. Binelli, D. Pinardi, T. Nili, and A. Farina, "Individualized HRTF for playing VR videos with Ambisonics spatial audio on HMDs," in *Proceedings of the AES International Conference*, 2018, vol. 2018-Augus.

[41] A. Farina, "Advancements in Impulse Response Measurements by Sine Sweeps," *Journal of The Audio Engineering Society*, 2007.

[42] A. Farina and E. Ugolotti, "Use of Digital Inverse Filtering Techniques for Improving Car Audio Systems," Nov. 2000.

[43] M. Binelli and A. Farina, *Digital Equalization of Automotive Sound Systems Employing Spectral Smoothed FIR Filters*. 2008.

[44] "COMSOL, Acoustics Module User's Guide."

[45] A. Tira, D. Pinardi, C. Belicchi, A. Farina, A. Figuretti, and S. Izzo, *Analytical and Numerical Models of the Sound Radiated by Fully Clamped Rectangular Vibrating Plates*. 2022. doi: 10.4271/2022-01-0973.

[46] L. Collini, A. Farina, R. Garziera, D. Pinardi, and K. Riabova, "Application of laser vibrometer for the study of loudspeaker dynamics," *Mater Today Proc*, vol. 4, no. 5, Part 1, pp. 5773–5778, 2017, doi: https://doi.org/10.1016/j.matpr.2017.06.044.

[47] N. Hosoya, I. Kajiwara, and T. Hosokawa, "Vibration testing based on impulse response excited by pulsed-laser ablation: Measurement of frequency response function with detection-free input," *J Sound Vib*, vol. 331, no. 6, pp. 1355–1365, 2012, doi: https://doi.org/10.1016/j.jsv.2011.10.034.

[48] L. Scislo, "Quality Assurance and Control of Steel Blade Production Using Full Non-Contact Frequency Response Analysis and 3D Laser Doppler Scanning Vibrometry System," in *2021 11th IEEE International Conference on Intelligent Data Acquisition and Advanced Computing Systems: Technology and Applications (IDAACS)*, 2021, vol. 1, pp. 419–423. doi: 10.1109/IDAACS53288.2021.9661060.

[49] L. Collini, A. Farina, R. Garziera, D. Pinardi, and K. Riabova, "Application of laser vibrometer for the study of loudspeaker dynamics," in *Materials Today: Proceedings*, 2017, vol. 4, no. 5. doi: 10.1016/j.matpr.2017.06.044.

[50] C. Belicchi *et al.*, *ANC: A Low-Cost Implementation Perspective*. 2022. doi: 10.4271/2022-01-0967.

[51] C. Tripodi *et al.*, "Experimental Results on Active Road Noise Cancellation in Car Interior," in *Audio Engineering Society Convention 144*, Oct. 2018. [Online]. Available: http://www.aes.org/e-lib/browse.cfm?elib=19493

[52] L. P. R. de Oliveira, P. S. Varoto, P. Sas, and W. Desmet, "A State-Space Modeling Approach for Active Structural Acoustic Control," *Shock and Vibration*, vol. 16, p. 797125, 2009, doi: 10.3233/SAV-2009-0492.

[53] X. Du, X. Liao, Q. Fu, and C. Zong, "Vibro-Acoustic Analysis of Rectangular Plate-Cavity Parallelepiped Coupling System Embedded with 2D Acoustic Black Holes," *Applied Sciences*, vol. 12, no. 9, 2022, doi: 10.3390/app12094097.

[54] S. Dhandole and S. v Modak, "Review of vibro-acoustics analysis procedures for prediction of low frequency noise inside a cavity," *Conference Proceedings of the Society for Experimental Mechanics Series*, Jan. 2007.

[55] A. Dowsett, D. O'Boy, S. Walsh, A. Abolfathi, and S. Fisher, "The prediction of measurement variability in an automotive application by the use of a coherence formulation," *Proceedings of the Institution of Mechanical Engineers, Part D: Journal of Automobile Engineering*, vol. 232, no. 12, pp. 1694–1700, Oct. 2017, doi: 10.1177/0954407017734768.

[56] S. Dhandole and S. v Modak, "Review of vibro-acoustics analysis procedures for prediction of low frequency noise inside a cavity," *Conference Proceedings of the Society for Experimental Mechanics Series*, Jan. 2007.

[57] M. E. Altınsoy and U. Jekosch, "The Semantic Space of Vehicle Sounds: Developing a Semantic Differential with Regard to Customer Perception," *Journal of The Audio Engineering Society*, vol. 60, pp. 13–21, Jan. 2012.

[58] E. A. Piana, A. C. Nilsson, and N. Granzotto, "Acoustic properties of composite lightweight structures," in *Euronoise 2015*, 2015, pp. 949 – 954. [Online]. Available: https://www.scopus.com/inward/record.uri?eid=2-s2.0-85080894881&partnerID=40&md5=f33722c44a0c3d6866fa62f21949da1b

[59] A. Nilsson, S. Baro, and E. A. Piana, "Vibro-acoustic properties of sandwich structures," *Applied Acoustics*, vol. 139, pp. 259 – 266, 2018, doi: 10.1016/j.apacoust.2018.04.039.

[60] N. Misdariis and L. Pardo, "The sound of silence of electric vehicles – Issues and answers," 2017.

[61] U. Orrenius and U. Carlsson, "Attractive Train Interiors: Minimizing Annoying Sound and Vibration," in *Notes on Numerical Fluid Mechanics and Multidisciplinary Design*, vol. 126, 2015, pp. 707–714. doi: 10.1007/978-3-662-44832-8_84.

[62] A. Chatterjee, V. Ranjan, M. S. Azam, and M. Rao, "Comparison for the Effect of Different Attachment of Point Masses on Vibroacoustic Behavior of Parabolic Tapered Annular Circular Plate," *Applied Sciences*, vol. 9, no. 4, 2019, doi: 10.3390/app9040745.

[63] N. Harris and M. Hawksford, "The Distributed-Mode Loudspeaker (DML) as a Broad-Band Acoustic Radiator," Jan. 2012.

[64] M. Heilemann, D. Anderson, S. Roessner, and M. Bocko, "The Evolution and Design of Flat-Panel Loudspeakers for Audio Reproduction," *Journal of the Audio Engineering Society*, vol. 69, pp. 27–39, Feb. 2021, doi: 10.17743/jaes.2020.0057.

[65] S. Cecchi, A. Terenzi, F. Piazza, and F. Bettarelli, *Applying Sound Equalization to Vibrating Sound Transducers Mounted on Rigid Panels*. 2019.

[66] J. Panzer and N. Harris, "Distributed-Mode Loudspeaker Radiation Simulation," *Journal of The Audio Engineering Society*, 1998.

[67] B. Pueo, J. Lopez, G. Ramos, and J. Escolano, "Efficient equalization of multi-exciter distributed mode loudspeakers," *Applied Acoustics*, vol. 70, pp. 737–746, May 2009, doi: 10.1016/j.apacoust.2008.09.005.

[68] M. Cho, E. Prokofieva, J. Munoz, and M. Barker, "Improvement of Sound Quality by Means of Ultra-Soft Elastomer for the Gel Type Inertia Driven

DML Type Transducer.," 2010. [Online]. Available: http://researchrepository.napier.ac.uk/id/eprint/6862

[69] D. Anderson, M. Heilemann, and M. Bocko, "Flat-Panel Loudspeaker Simulation Model with Electromagnetic Inertial Exciters and Enclosures," *Journal of the Audio Engineering Society*, vol. 65, pp. 722–732, Sep. 2017, doi: 10.17743/jaes.2017.0027.

ACKNOWLEDGEMENTS

This research was funded by McLaren Automotive, to which I am grateful.